Journal of Computational Physics 229 (2010) 4033–4058

Contents lists available at ScienceDirect

Journal of Computational Physics

journal homepage: www.elsevier.com/locate/jcp

High order well-balanced finite volume schemes for simulating wave propagation in stratified magnetic atmospheres

F.G. Fuchs [a], A.D. McMurry [a], S. Mishra [a], N.H. Risebro [a], K. Waagan [b,*]

[a] Centre of Mathematics for Applications (CMA), University of Oslo, P.O. Box 1053, Blindern, N-0316 Oslo, Norway
[b] High Altitude Observatory (HAO), National Center of Atmospheric Research, P.O. Box 3000, Boulder, 80307-3000 Colorado, USA

ARTICLE INFO

Article history:
Received 14 May 2009
Received in revised form 31 December 2009
Accepted 28 January 2010
Available online 14 February 2010

Dedicated with appreciation to Prof. Winther on his 60th Birthday

Keywords:
Conservation laws
MHD
Divergence constraint
Upwinded source terms

ABSTRACT

Wave propagation in idealized stellar atmospheres is modeled by the equations of ideal MHD, together with the gravity source term. The waves are modeled as small perturbations of isothermal steady states of the system. We consider a formulation of ideal MHD based on the Godunov–Powell form, with an embedded potential magnetic field appearing as a parameter. The equations are discretized by finite volume schemes based on approximate Riemann solvers of the HLL type and upwind discretizations of the Godunov–Powell source terms. Local hydrostatic reconstructions and suitable discretization of the gravity source term lead to a well-balanced scheme, i.e., a scheme which exactly preserves a discrete version of the relevant steady states. Higher order of accuracy is obtained by employing suitable minmod, ENO and WENO reconstructions, based on the equilibrium variables, to construct a well-balanced scheme. The resulting high order well-balanced schemes are validated on a suite of numerical experiments involving complex magnetic fields. The schemes are observed to be robust and resolve the complex physics well.

1. Introduction

The problem of modeling wave propagation in idealized stellar atmospheres has received considerable attention in the solar physics and astrophysics communities in recent years (see [42,6] and references therein). A typical situation of interest is to model how convection generated waves from the inner layers of the sun transport and deposit energy in the overlaying chromospheric and coronal plasmas. The waves interact with complex magnetic fields generated by the plasma and these interactions affect the qualitative as well as quantitative features of the energy transfer.

In [42,6], these complex phenomena were modeled in terms of the equations of magnetohydrodynamics (MHD) in two space dimensions, together with a gravitational source term given by

$$\begin{aligned}
&\rho_t + \operatorname{div}(\rho\mathbf{u}) = 0,\\
&(\rho\mathbf{u})_t + \operatorname{div}\Big(\rho\mathbf{u}\otimes\mathbf{u} + \Big(p + \tfrac{1}{2}|\overline{\mathbf{B}}|^2\Big)I - \overline{\mathbf{B}}\otimes\overline{\mathbf{B}}\Big) = -\rho g\mathbf{e}_2,\\
&\overline{\mathbf{B}}_t + \operatorname{div}(\mathbf{u}\otimes\overline{\mathbf{B}} - \overline{\mathbf{B}}\otimes\mathbf{u}) = 0,\\
&E_t + \operatorname{div}\Big(\Big(E + p + \tfrac{1}{2}|\overline{\mathbf{B}}|^2\Big)\mathbf{u} - (\mathbf{u}\cdot\overline{\mathbf{B}})\overline{\mathbf{B}}\Big) = -\rho g(\mathbf{u}\cdot\mathbf{e}_2),\\
&\operatorname{div}(\overline{\mathbf{B}}) = 0,
\end{aligned} \tag{1.1}$$

* Corresponding author.
E-mail addresses: franzf@math.uio.no (F.G. Fuchs), a.d.mcmurry@ifi.uio.no (A.D. McMurry), siddharm@cma.uio.no (S. Mishra), nilshr@math.uio.no (N.H. Risebro), knutwa@ucar.edu (K. Waagan).
URL: http://folk.uio.no/franzf/ (F.G. Fuchs).

0021-9991/$ - see front matter © 2010 Elsevier Inc. All rights reserved.
doi:10.1016/j.jcp.2010.01.038

where ρ is the density, $\mathbf{u} = \{u_1, u_2, u_3\}$ and $\overline{\mathbf{B}} = \{\overline{B}_1, \overline{B}_2, \overline{B}_3\}$ are the velocity and magnetic fields respectively, p is the thermal pressure, g is constant acceleration due to gravity , $\mathbf{e}_2$ represents the unit vector in the vertical (y)-direction. E is the total energy, for simplicity determined by the ideal gas equation of state:

$$E = \frac{p}{\gamma - 1} + \frac{1}{2}\rho|\mathbf{u}|^2 + \frac{1}{2}|\overline{\mathbf{B}}|^2, \tag{1.2}$$

where $\gamma > 1$ is the adiabatic gas constant. The above equations represent the conservation of mass, momentum and energy and the magnetic induction equations for the evolution of the magnetic field. The momentum conservation is affected by the Lorentz force due to the magnetic field and by the gravitational force. The total energy is the sum of the energy due to the pressure and the kinetic and magnetic energies. The gravitational potential energy is modeled by the source term on the right hand side of the energy equation. The divergence constraint on the magnetic field reflects the fact that magnetic monopoles have not been observed in nature.

The above Eq. (1.1) posses a rich variety of steady states that are of interest in modeling wave propagation. Two interesting steady states considered in [42,6] and in a recent paper [18] are given as follows.

1.1. Hydrodynamic steady state

This steady state assumes that the velocity $\mathbf{u}$ and magnetic field $\overline{\mathbf{B}}$ are set to zero. Furthermore, we are interested in chromospheric plasmas where the temperature is approximately constant ([6]) and one can assume that the atmosphere is isothermal. A simple calculation ([18]) with the above assumptions leads to the following steady (or more precisely, static) state:

$$\mathbf{u} \equiv 0, \quad \overline{\mathbf{B}} \equiv 0, \quad \rho(x,y) = \rho_0 e^{-y/H}, \quad p(x,y) = p_0 e^{-y/H}, \tag{1.3}$$

where the scale height H is given by $H = p_0/g\rho_0$ and p_0 and ρ_0 are the values of the pressure and density at the bottom boundary of the domain. Note that the hydrostatic balance due to gravity implies that the pressure and the density decay exponentially in the vertical direction. Hence, very low pressures and densities can be found at the top of the domain of interest.

1.2. Magnetic steady state

The hydrodynamic steady state assumes that the magnetic field is zero. Any realistic description of solar plasmas cannot ignore the effect of magnetic field since it plays a crucial role in the energy transfer [6]. Steady states with a magnetic field are easy to determine once the momentum balance in (1.1) is rewritten as

$$(\rho\mathbf{u})_t + \operatorname{div}(\rho\mathbf{u} \otimes \mathbf{u} + pI) = \operatorname{curl}(\overline{\mathbf{B}}) \times \overline{\mathbf{B}} - \rho g \mathbf{e}_2.$$

The above equation displays the role of the Lorentz force explicitly in the momentum balance. Under the assumption that the velocity field is set to zero, the following magnetic steady states are easy to obtain,

$$\begin{aligned} &\mathbf{u} \equiv 0, \quad \operatorname{div}(\overline{\mathbf{B}}) \equiv 0, \quad \operatorname{curl}(\overline{\mathbf{B}}) \equiv 0, \\ &\rho(x,y) = \rho_0 e^{-y/H}, \quad p(x,y) = p_0 e^{-y/H}. \end{aligned} \tag{1.4}$$

The above conditions require that the magnetic field is both divergence free and curl free. It is easy to obtain closed form solutions of such magnetic fields in terms of harmonic functions ([18] and in Section 2). Note that the conditions on steady magnetic fields are quite general and imply that there is a rich variety of magnetic steady states (1.4).

The usual method in modeling waves is to consider them as small perturbations of the above steady states. The Eq. (1.1) are supplemented with the steady states (1.3), (1.4) as initial conditions. Since, we are interested in a small part of the solar atmosphere, periodic boundary conditions are imposed in the horizontal (x)-direction. The waves are pushed into the domain by imposing suitable inflow boundary conditions at the bottom boundary. One expects the wave forms to be distorted due to interactions with the magnetic field and the action of gravity. The distorted waves exit the domain through the top boundary. The top boundary is an artificial boundary and suitable numerical boundary conditions need to be imposed in order to ensure that the waves exit the domain without large reflections.

Equations of form (1.1) are examples of systems of balance laws (conservation laws with source terms). Solutions of such equations develop discontinuities such as shock waves and contact discontinuities, even for smooth initial data. Hence, solutions have to be considered in the weak sense. The MHD equations are hyperbolic but not strictly hyperbolic, since different characteristic speeds can coincide.

If the eigenvectors of the Jacobian matrix of the flux functions are to be used in computations, then these must be suitably scaled (see [41,3] for detailed descriptions). The structure of discontinuities of the MHD equations is quite complicated as the flux functions are non-convex [50].

We remark that (even in one space dimension) global existence and uniqueness results have not been obtained at the current time.

Hence, numerical simulations of these equations is the main tool of study and analysis. Finite volume methods [29] are among the most popular tools for discretizing non-linear balance laws like (1.1). The computational domain is divided into control volumes or cells. The method consists of discretizing an integral version of a balance law like (1.1) over each cell to obtain a time update of the cell averages of the unknown. The key step in the update is to determine numerical fluxes by solving local Riemann problems at each cell interface (along the normal direction). The source term in the balance law (1.1) can be discretized in several ways. Higher order accuracy in space can be obtained by using non-oscillatory piecewise polynomial reconstructions like the MUSCL [52], ENO [24] and WENO [45] reconstructions. High order temporal accuracy is obtained by using strong stability preserving Runge–Kutta methods [23].

Finite volume schemes for ideal MHD equations have undergone considerable development in the last fifteen years. In one space dimension, finite volume schemes for MHD equations include the linearized solvers developed in [41,10]. Other schemes are the non-linear HLL type solvers designed in [31,22,36,7,8,17] and references therein. The linearized Roe-type solvers are less dissipative than the HLL type solver but can lead to unphysical negative densities and pressures. The non-linear HLL type solvers like the ones designed in [22,36,7] are proved to preserve positive densities and pressures. Comparisons between different approximate Riemann solvers are performed in papers like [18,46,34].

In one space dimension, the divergence constraint in (1.1) implies that the normal magnetic field is constant in space. This information is used in the design of some of the above approximate Riemann solvers. However, the nature of MHD equations in multi space dimensions is different. The divergence constraint in several dimensions does not imply that the normal magnetic field is constant. Hence, it is not straightforward to extend one dimensional MHD schemes to several dimensions.

It is also difficult to satisfy the divergence constraint itself. Standard schemes may not preserve the constraint in a discrete manner and divergence errors are speculated to lead to numerical instabilities and unphysical oscillations [51]. Several methods have been designed to deal with the divergence constraint in MHD codes. Popular choices include the projection method, in which the magnetic field is projected into a zero divergence field by solving an elliptic equation at each time step [9], a method which is computationally expensive. A cheaper alternative is the parabolic cleaning method of [33,13]. Another popular method of handling the divergence constraint is the use of staggered grids to ensure that a particular form of discrete divergence is zero. Several versions of staggered grid methods exist, and an incomplete list includes those developed in [2,12,15,32,44,43,46,49,51] and other references therein. A possible disadvantage of staggered grid methods is the complexity of the book-keeping at the code level, leading to overheads in parallelizing the code. It is also more difficult to obtain numerical stability for these schemes, since some of the theoretical basis of finite volume schemes is lost.

A different divergence cleaning procedure was presented in [39,40] where a slightly different form of the ideal MHD equations (with a source term proportional to divergence) was discretized. This form, also called the *Godunov–Powell* form happens to be symmetrizable [21] and Galilean invariant, while the standard form (1.1) is neither symmetrizable nor Galilean invariant. Furthermore, in the Godunov–Powell form divergence errors are transported out of the domain with the flow ([39]). Similar ideas were presented in [13]. A possible pitfall of this procedure was pointed out in recent papers [16,17]. Examples were presented to argue that the Godunov–Powell form needs to be discretized in a suitable manner for numerical stability. Various upwind discretizations of a partial form of the Godunov–Powell source term were proposed recently in [7,53,17].

The Godunov–Powell form makes it mathematically feasible to deal with data not satisfying the divergence constraint. Hence, it allows constructing one dimensional schemes that immediately extend to accurate and remarkably robust multi-dimensional schemes, as carried out by the authors in [19] (see also [53]). The method involved designing suitable three and five wave HLL type solvers and discretizing the Godunov–Powell source term in an upwind manner. The source discretization involved utilizing the structure of the approximate Riemann solver. Positivity preserving high order ENO and WENO reconstructions were also proposed. The resulting schemes were high order accurate and robust in computations, particularly on very fine meshes. The numerical schemes designed in [19] constitute an attractive framework for robust simulations of models involving MHD equations.

In order to extend existing finite volume methods for the ideal MHD equations to the balance law (1.1), we need to discretize the terms due to gravity in a suitable manner. The resulting scheme should be able to handle very low pressures and densities (see the exponential structure in (1.4) at the top of the domain. Furthermore, waves are very small perturbations of the steady states (1.3), (1.4), so resolving them requires that the scheme approximating (1.1) preserves discrete versions of the steady states (1.3), (1.4) to sufficient accuracy. Another hurdle is the issue of suitable numerical boundary conditions at the top boundary. This boundary condition must ensure mass balance and low reflections.

A recent paper [18] illustrated some of the problems in extending existing finite volume methods to simulate wave propagation involving models like (1.1). In [18], the gravity source term was discretized by a fractional steps method [29] and characteristic type boundary conditions [38,48] were used at the top boundary. However, these methods led to significant numerical instabilities and large boundary reflections, particularly on problems with strong magnetic fields. In fact, *none* of the schemes considered in [18] were stable on wave propagation problems with strong magnetic fields. The lack of robust finite volume schemes preserving discrete steady states was a persistent problem.

Finite volume methods which preserve steady states in balance laws are called *well-balanced*. Many balance laws like shallow water equations with bottom topography [30] and Euler equations for gas flows in nozzles [28] involve balance laws with interesting steady states. Well-balanced schemes for the shallow water equations with topography have been designed in many recent papers including [30,1,37,11] and other references therein. Well-balanced schemes for nozzle flows are considered in [27,28] among others. The most popular form of well-balancing a scheme is to use local *hydrostatic*

reconstructions. A different approach is considered in [25]. To the best of our knowledge, no well-balanced schemes for simulating wave propagation in stratified atmospheres has been designed, even in the absence of magnetic fields.

The aim of this paper is to design a robust finite volume scheme to simulate waves modeled as perturbations of steady states (1.3), (1.4) in the balance law (1.1). Our approach consists of the following ingredients,

- We follow the approach of [47,40] and consider a modified formulation of the balance law (1.1). The modified form includes the Godunov–Powell source term discussed earlier. It also considers an embedded steady magnetic field like (1.4) and solves for the deviation of this magnetic field, which is treated as a parameter. This approach is motivated by the fact that we are interested in small perturbations of the steady magnetic field (1.4).
- The resulting modified MHD system is discretized by a finite volume method, similar to the schemes of [19]. The numerical fluxes are calculated by a suitable three wave approximate Riemann solver of the HLL type. The Godunov–Powell term is discretized in an upwind fashion. Minmod, ENO and WENO reconstructions are used to obtain higher order accuracy.
- A novel form of well-balancing is designed by using suitable local hydrostatic reconstructions in the numerical fluxes. The gravity source term is also well-balanced. Novel piecewise linear reconstructions are proposed to obtain a second-order accurate well-balanced scheme.
- Well-balanced Neumann type boundary conditions are proposed to reduce reflections and ensure stability at the top boundary. These conditions are very similar to the extrapolated Neumann boundary conditions of [18].

The above ingredients are combined to obtain robust well-balanced high order finite volume schemes for wave propagation in stratified magneto-atmospheres. The schemes are tested on a suite of numerical experiments including perturbations of hydrodynamic steady states (1.3). However, the main interest is to study wave propagation as perturbations of the magnetic steady states (1.4). We consider realistic background magnetic fields and simulate wave propagation. The numerical results illustrate both accuracy and stability of the schemes. The schemes are employed to describe complex physical phenomena accompanying wave propagation. Particular attention is paid to examine the role of magnetic fields in influencing wave propagation. The numerical results show qualitative agreement with the ones presented in [6], and demonstrate considerable improvements over the results of [6] with respect to modeling very small perturbations of steady states, long time integration and interaction of waves with the top boundary.

The remaining part of the paper is organized as follows: in Section 2, we describe a modified formulation of (1.1). The high order accurate well-balanced schemes are presented in Section 3. In Section 4, we present various numerical experiments demonstrating the computational efficiency of the schemes. We describe some of the complex physical phenomena underlying wave propagation in this section. Contents of the papers are summarized in Section 5.

2. The model

Deriving the ideal MHD equations with gravity (1.1) from the first principles without explicitly using the divergence constraint results in the following semi-conservative *Godunov–Powell* form of the equations (see [19] for a detailed derivation in the absence of gravity),

$$\begin{aligned}
&\rho_t + \operatorname{div}(\rho\mathbf{u}) = 0,\\
&(\rho\mathbf{u})_t + \operatorname{div}\left(\rho\mathbf{u}\otimes\mathbf{u} + \left(p + \frac{1}{2}|\bar{\mathbf{B}}|^2\right)I - \overline{\mathbf{B}}\otimes\overline{\mathbf{B}}\right) = -\overline{\mathbf{B}}(\operatorname{div}\overline{\mathbf{B}}) - \rho g\mathbf{e}_2,\\
&\overline{\mathbf{B}}_t + \operatorname{div}(\mathbf{u}\otimes\overline{\mathbf{B}} - \overline{\mathbf{B}}\otimes\mathbf{u}) = -\mathbf{u}(\operatorname{div}\overline{\mathbf{B}}),\\
&\bar{E}_t + \operatorname{div}\left(\left(E + p + \frac{1}{2}|\bar{\mathbf{B}}|^2\right)\mathbf{u} - (\mathbf{u}\cdot\bar{\mathbf{B}})\overline{\mathbf{B}}\right) = -(\mathbf{u}\cdot\overline{\mathbf{B}})(\operatorname{div}\overline{\mathbf{B}}) - \rho g(\mathbf{u}\cdot\mathbf{e}_2).
\end{aligned} \tag{2.1}$$

The system is coupled with an ideal gas equation of state (1.2) and all the quantities in (2.1) are as defined before. The difference between the standard form (1.1) and the Godunov–Powell form (2.1) are the explicitly div $\overline{\mathbf{B}}$-dependent source terms in (2.1). Taking divergence on both sides of (2.1), we obtain

$$(\operatorname{div}\overline{\mathbf{B}})_t + \operatorname{div}(\mathbf{u}(\operatorname{div}\overline{\mathbf{B}})) = 0. \tag{2.2}$$

Hence, initial divergence free fields remain divergence free under time evolution in (2.1). Furthermore, the Godunov–Powell system is Galilean invariant [40] and symmetrizable [21]. Hence, our starting point will be the Godunov–Powell form (2.1) instead of the standard form (1.1).

Motivated by our interest in modeling wave propagation as perturbations of steady states (1.3), (1.4), we consider a further modification of the system (2.1). Assume that there exist a magnetic field $\widetilde{\mathbf{B}}$ satisfying the following assumptions,

$$\widetilde{\mathbf{B}}_t = 0, \quad \operatorname{div}(\widetilde{\mathbf{B}}) = 0, \text{ and } \operatorname{curl}(\widetilde{\mathbf{B}}) = 0. \tag{2.3}$$

Specific examples of such fields will be given in the sequel. Next, we define the deviation $\mathbf{B}$ about this potential field $\widetilde{\mathbf{B}}$ by,

$$\mathbf{B} = \overline{\mathbf{B}} - \widetilde{\mathbf{B}}.$$

We plug in the above form in (2.1) and after some calculations (see [40]), we obtain the following modified system,

$$\begin{aligned}
&\rho_t + \operatorname{div}(\rho\mathbf{u}) = 0,\\
&(\rho\mathbf{u})_t + \operatorname{div}\left(\rho\mathbf{u}\otimes\mathbf{u} + \left(p + \frac{1}{2}|\mathbf{B}|^2 + \widetilde{\mathbf{B}}\cdot\mathbf{B}\right)I - \mathbf{B}\otimes\mathbf{B} - \widetilde{\mathbf{B}}\otimes\mathbf{B} - \mathbf{B}\otimes\widetilde{\mathbf{B}}\right) = -(\mathbf{B}+\widetilde{\mathbf{B}})(\operatorname{div}\mathbf{B}) - \rho g\mathbf{e}_2,\\
&\mathbf{B}_t + \operatorname{div}(\mathbf{u}\otimes\mathbf{B} - \mathbf{B}\otimes\mathbf{u} + \mathbf{u}\otimes\widetilde{\mathbf{B}} - \widetilde{\mathbf{B}}\otimes\mathbf{u}) = -\mathbf{u}(\operatorname{div}\mathbf{B}),\\
&E_t + \operatorname{div}\left(\left(E + p + \frac{1}{2}|\mathbf{B}|^2 + \mathbf{B}\cdot\widetilde{\mathbf{B}}\right)\mathbf{u} - (\mathbf{u}\cdot\mathbf{B})\mathbf{B} - (\mathbf{u}\cdot\widetilde{\mathbf{B}})\mathbf{B}\right) = -(\mathbf{u}\cdot\mathbf{B})(\operatorname{div}\mathbf{B}) - \rho g(\mathbf{u}\cdot\mathbf{e}_2),
\end{aligned} \tag{2.4}$$

where $E = \frac{p}{\gamma-1} + \frac{1}{2}|\mathbf{B}|^2 + \frac{1}{2}\rho|\mathbf{u}|^2$. The variable of interest is now the deviation magnetic field $\mathbf{B}$ and the background magnetic field $\widetilde{\mathbf{B}}$ satisfying (2.3) appears as a parameter in the above equations.

Remark 2.1. The only assumptions used in deriving (2.4) are given by (2.3). In particular, no linearization assumptions were made nor was any condition imposed on the magnitude of $\mathbf{B}$. Hence, the above Eq. (2.4) can be thought of as another equivalent form of the MHD equations with gravity (1.1).

We will discretize the above Eq. (2.4) in the remaining part of this paper. Writing (2.4) explicitly in two space dimensions results in

$$\mathbf{U}_t + (\mathbf{f}(\mathbf{U},\widetilde{\mathbf{B}})_x + \mathbf{g}(\mathbf{U},\widetilde{\mathbf{B}})_y = \mathbf{s}^1(\mathbf{U},\widetilde{\mathbf{B}}) + \mathbf{s}^2(\mathbf{U},\widetilde{\mathbf{B}}) + \mathbf{s}^g(\mathbf{U}), \tag{2.5}$$

where

$$\mathbf{U} = \{\rho, \rho u_1, \rho u_2, \rho u_3, B_1, B_2, B_3, E\},$$

is the vector of conserved variables and $\widetilde{\mathbf{B}} = \{\widetilde{B}_1, \widetilde{B}_2, \widetilde{B}_3\}$ is any background magnetic field defined by (2.4). The above form clearly illustrates that the fluxes and the Godunov–Powell source term depend on the parameter $\widetilde{B}$. Hence, (2.5) is an example of a balance law with spatially varying parameters. Such equations have many interesting properties (see [35]) for a detailed exposition). The fluxes in (2.5) are given by

$$\mathbf{f} = \begin{pmatrix}
\rho u_1\\
\rho u_1^2 + \pi_1 - \frac{B_1^2}{2} - \widetilde{B}_1 B_1\\
\rho u_1 u_2 - B_1 B_2 - \widetilde{B}_1 B_2 - B_1\widetilde{B}_2\\
\rho u_1 u_3 - B_1 B_3 - \widetilde{B}_1 B_3 - B_1\widetilde{B}_3\\
0\\
u_1(B_2 + \widetilde{B}_2) - u_2(B_1 + \widetilde{B}_1)\\
u_1(B_3 + \widetilde{B}_3) - u_3(B_3 + \widetilde{B}_3)\\
(E + \pi_1)u_1 - u_1\frac{B_1^2}{2} - (B_1 + \widetilde{B}_1)(u_2 B_2 + u_3 B_3)
\end{pmatrix},$$

$$\mathbf{g} = \begin{pmatrix}
\rho u_2\\
\rho u_1 u_2 - B_1 B_2 - \widetilde{B}_1 B_2 - B_1\widetilde{B}_2\\
\rho u_2^2 + \pi_2 - \frac{B_2^2}{2} - \widetilde{B}_2 B_2\\
\rho u_2 u_3 - B_2 B_3 - \widetilde{B}_2 B_3 - B_2\widetilde{B}_3\\
0\\
u_2(B_2 + \widetilde{B}_2) - u_2(B_2 + \widetilde{B}_2)\\
u_2(B_3 + \widetilde{B}_3) - u_3(B_3 + \widetilde{B}_3)\\
(E + \pi_2)u_2 - u_2\frac{B_2^2}{2} - (B_2 + \widetilde{B}_2)(u_2 B_2 + u_3 B_3)
\end{pmatrix}, \tag{2.6}$$

where we have defined

$$\pi_1 = p + \frac{B_2^2 + B_3^2}{2} + B_2\widetilde{B}_2 + B_3\widetilde{B}_3, \quad \pi_2 = p + \frac{B_1^2 + B_3^2}{2} + B_1\widetilde{B}_1 + B_3\widetilde{B}_3. \tag{2.7}$$

Similarly, the Godunov–Powell source terms in (2.1) can be written explicitly as

$$\mathbf{s}^1 = \begin{pmatrix} 0, \\ -\left(\frac{B_1^2}{2}\right)_x - \widetilde{B}_1(B_1)_x \\ -(B_2+\widetilde{B}_2)(B_1)_x \\ -(B_3+\widetilde{B}_3)(B_1)_x \\ -u_1(B_1)_x \\ -u_2(B_1)_x \\ -u_3(B_1)_x \\ -u_1\left(\frac{B_1^2}{2}\right)_x - (u_2B_2+u_3B_3)(B_1)_x \end{pmatrix} \quad \mathbf{s}^2 = \begin{pmatrix} 0, \\ -(B_1+\widetilde{B}_1)(B_2)_y \\ -\left(\frac{B_2^2}{2}\right)_y - \widetilde{B}_2(B_2)_y \\ -(B_3+\widetilde{B}_3)(B_2)_y \\ -u_1(B_2)_y \\ -u_2(B_2)_y \\ -u_3(B_2)_y \\ -u_2\left(\frac{B_2^2}{2}\right)_y - (u_1B_1+u_3B_3)(B_2)_y \end{pmatrix}. \tag{2.8}$$

Note that we have used the chain rule $B_1(B_1)_x = \left(\frac{B_1^2}{2}\right)_x$ as well as a similar rule for the product $B_2(B_2)_y$. While true for smooth solutions, this formula may no longer hold when the magnetic field has discontinuities. However, choosing this definition of the non-conservative product was found to be robust in practice (see [19]).

Finally, the gravitational source term is given by

$$\mathbf{s}^g = \{0, 0, -\rho g, 0, 0, 0, 0, -\rho u_2 g\}. \tag{2.9}$$

Considering the primitive variables $\mathbf{V} = \{\rho, \mathbf{u}, \mathbf{B}, p\}$, we can write (2.5) in the quasilinear form

$$\mathbf{V}_t + A\mathbf{V}_x + B\mathbf{V}_y = \widetilde{\mathbf{S}},$$

where $(A, B) = (\partial_{\mathbf{U}}\mathbf{f}, \partial_{\mathbf{U}}\mathbf{g})$ are the flux Jacobians. Set $\overline{\mathbf{B}} = \mathbf{B} + \widetilde{\mathbf{B}}$, denoting the sound speed $a^2 = \frac{\gamma p}{\rho}$ and $b_{1,2,3} = \frac{\overline{\mathbf{B}}_{1,2,3}}{\sqrt{\rho}}$, $b^2 = b_1^2 + b_2^2 + b_3^2$, the eigenvalues of A are calculated (see [40]) as

$$\begin{aligned} &\lambda_1 = u_1 - c_f, \quad \lambda_2 = u_1 - b_1, \quad \lambda_3 = u_1 - c_s, \quad \lambda_4 = u_1, \\ &\lambda_5 = u_1, \quad \lambda_6 = u_1 + c_s, \quad \lambda_7 = u_1 + b_1, \quad \lambda_8 = u_1 + c_f, \end{aligned} \tag{2.10}$$

where c_f, c_s are given by

$$c_f^2 = \frac{1}{2}\left(a^2 + b^2 + \sqrt{(a^2+b^2)^2 - 4a^2b_1^2}\right), \quad c_s^2 = \frac{1}{2}\left(a^2 + b^2 - \sqrt{(a^2+b^2)^2 - 4a^2b_1^2}\right).$$

The waves corresponding to λ_1, λ_8 are termed as fast waves, ones corresponding to λ_3, λ_6 as slow waves, those corresponding to λ_2, λ_7 as Alfvén waves and the wave associated with $\lambda_{4,5}$ is a contact or shear wave. Note that the parameter $\widetilde{\mathbf{B}}$ enters into the expressions of the eigenvalues. The eigenvalues of B (in the y-direction) are analogously defined.

2.1. Steady states

As in the introduction, we assume that $\mathbf{u} \equiv 0$ and that $\widetilde{\mathbf{B}}$ satisfies the potential field assumptions (2.3). Furthermore if the deviation $\mathbf{B} \equiv 0$ and an isothermal atmosphere is assumed, i.e. $p = C\rho$ for some constant C, then simple calculations (see [18]) lead to the following steady states of (2.4),

$$\mathbf{u} = 0, \quad \mathbf{B} = 0, \quad \rho(x,y) = \rho_0 e^{-y/H}, \quad p(x,y) = p_0 e^{-y/H}, \tag{2.11}$$

where the scale height H is given by $H = p_0/g\rho_0$ and p_0 and ρ_0 are the values of the pressure and density at the bottom boundary of the domain. Observe that the above steady state is magnetostatic, since only the perturbation $\mathbf{B}$ is assumed to be zero. The magnetic field is manifest in (2.11) through the background field $\widetilde{\mathbf{B}}$.

2.1.1. Hydrodynamic steady state

So far, the background field $\widetilde{\mathbf{B}}$ only satisfies (2.3). Specific solutions of the assumptions (2.3) lead to a classification of possible steady states. The simplest solution of (2.3) is given by

$$\widetilde{\mathbf{B}} \equiv 0. \tag{2.12}$$

The steady state (2.11) together with zero background field (2.12) is referred to as the hydrodynamic steady state. It is equivalent to the hydrodynamic steady state (1.3) of (1.1).

2.1.2. Magnetic steady states

Non-trivial solutions of (2.3) lead to an interesting magnetic steady states. Note that solutions of (2.3) can be characterized by vector harmonic functions. We use the following Fourier expansion of vector harmonic functions (see also [18]),

$$B_1(x,y)=\sum_{k=0}^{M} f_k \sin\left(\frac{2k\pi x}{X}\right)e^{-\frac{2\pi k y}{X}},\quad B_2(x,y)=\sum_{k=0}^{M} f_k \cos\left(\frac{2k\pi x}{X}\right)e^{-\frac{2\pi k y}{X}},\quad B_3(x,y)\equiv 0, \tag{2.13}$$

where the f_k's are Fourier coefficients corresponding to the background magnetic field at the bottom of the domain and M is total number of Fourier modes. The constant X in (2.13) refers to the length of the domain (in the x-direction) under consideration. Note that the above field (2.13) can be quite complicated with a large number of modes. However, even more general solutions of (2.3) can be found, particularly those with non-zero B_3. We restrict ourselves to fields of the form (2.13) in our numerical simulations. The steady state (2.11) with a background field like (2.13) is called a magnetic steady state.

Remark 2.2. A big advantage of using the modified formulation (2.4) is that it allows for a unified treatment of steady states. Observe that all isothermal steady states of (2.4) are given by (2.11). The difference between individual steady states lies in the choice of the background field $\widetilde{\mathbf{B}}$. This enables us to use a single characterization of isothermal steady states and design well-balanced schemes which preserve them.

3. Numerical schemes

For notational simplicity, we focus on the MHD Eq. (2.1) in two space dimensions. The extension to three space dimensions is straightforward. We approximate (2.5) in a domain $\mathbf{x}=(x,y)\in[X_l,X_r]\times[Y_b,Y_t]$. For simplicity, the domain is discretized by a uniform grid in both directions with the grid spacing Δx and Δy. We set $x_i=X_l+i\Delta x$ and $y_j=Y_b+j\Delta y$. The indices are $0\leqslant i\leqslant N_x$ and $0\leqslant j\leqslant N_y$. Set $x_{i+1/2}=x_i+\Delta x/2$ and $y_{j+1/2}=y_j+\Delta y/2$, and let $I_{ij}=[x_{i-1/2},x_{i+1/2})\times[y_{j-1/2},y_{j+1/2})$ denote a typical cell. The cell average of the unknown state vector $\mathbf{W}$ (approximating $\mathbf{U}$) over I_{ij} at time t^n is denoted $\mathbf{W}_{ij}^n$.

3.1. First-order schemes

A standard finite volume scheme (first-order in both space and time) (see [29]) is obtained by integrating the balance law (2.5) over the cell I_{ij} and the time interval $[t^n,t^{n+1})$ with $t^{n+1}=t^n+\Delta t^n$, where the time-step Δt^n is determined by a suitable CFL condition. The resulting fully-discrete form of the scheme is

$$\mathbf{W}_{ij}^{n+1}=\mathbf{W}_{ij}^n-\frac{\Delta t^n}{\Delta x}\left(\mathbf{F}_{i+1/2,j}^n-\mathbf{F}_{i-1/2,j}^n\right)-\frac{\Delta t^n}{\Delta y}\left(\mathbf{G}_{ij+1/2}^n-\mathbf{G}_{ij-1/2}^n\right)+\Delta t^n\left(\mathbf{S}_{ij}^{1,n}+\mathbf{S}_{ij}^{2,n}+\mathbf{S}_{ij}^{g,n}\right). \tag{3.1}$$

The numerical fluxes $\mathbf{F}$, $\mathbf{G}$ and discretized sources $\mathbf{S}^1,\mathbf{S}^2$ and $\mathbf{S}^g$ are specified in the following sections.

3.1.1. Numerical flux and Godunov–Powell source in the x-direction

As in [19], we determine the numerical flux $\mathbf{F}_{i+1/2,j}^n$ and the source term $\mathbf{S}_{ij}^{1,n}$ from the (approximate) solution of the following Riemann problem

$$\mathbf{W}_t+\mathbf{f}(\mathbf{W},\widetilde{\mathbf{B}}_M)_x=\mathbf{s}^1(\mathbf{W},\widetilde{\mathbf{B}}_M,\mathbf{W}_x),\quad \mathbf{W}(x,0)=\begin{cases}\mathbf{W}_L & x<0,\\ \mathbf{W}_R & x>0,\end{cases} \tag{3.2}$$

where $\mathbf{f}$ and $\mathbf{s}^1$ are defined in (2.6) and (2.8) respectively. The Riemann initial data in terms of primitive variables are

$$\mathbf{V}_L=\left\{\rho_{ij}^n,\mathbf{u}_{ij}^n,\mathbf{B}_{ij}^n,p_{ij}^n\right\},\quad \mathbf{V}_R=\left\{\rho_{i+1,j}^n,\mathbf{u}_{i+1,j}^n,\mathbf{B}_{i+1,j}^n,p_{i+1,j}^n\right\}. \tag{3.3}$$

The data $\mathbf{W}_L,\mathbf{W}_R$ (in terms of conservative variables) is easily obtained from the primitive variables. The parameter $\widetilde{\mathbf{B}}_M$ in (3.2) is given by the average,

$$\widetilde{\mathbf{B}}_M=\widetilde{\mathbf{B}}_{i+1/2,j}=\frac{\widetilde{\mathbf{B}}_{ij}+\widetilde{\mathbf{B}}_{i+1,j}}{2}. \tag{3.4}$$

Hence, we stagger the parameter $\widetilde{\mathbf{B}}$ in defining the approximate Riemann solver. This approach is a popular discretization of balance laws with coefficients [26] and results in a simplification of the Riemann problem.

3.1.2. The HLL three wave solver

There are eight possible waves in the exact solution of the Riemann problem (3.2). We will approximate these eight waves with three waves, i.e. two representing the outermost fast waves and a middle wave approximating the material contact discontinuity. This approximate solution and fluxes for (3.2) are given by

$$\mathbf{W}^{H_3}=\begin{cases}\mathbf{W}_L & \text{if } \frac{x}{t}\leqslant s_L,\\ \mathbf{W}_L^* & \text{if } s_L<\frac{x}{t}<s_M,\\ \mathbf{W}_R^* & \text{if } s_M<\frac{x}{t}<s_R,\\ \mathbf{W}_R & \text{if } s_R\leqslant\frac{x}{t},\end{cases}\quad \mathbf{F}^{H_3}(\mathbf{W}_L,\mathbf{W}_R,\widetilde{\mathbf{B}}_M)=\begin{cases}\mathbf{F}_L & \text{if } \frac{x}{t}\leqslant s_L,\\ \mathbf{F}_L^* & \text{if } s_L<\frac{x}{t}<s_M,\\ \mathbf{F}_R^* & \text{if } s_M<\frac{x}{t}<s_R,\\ \mathbf{F}_R & \text{if } s_R\leqslant\frac{x}{t}.\end{cases} \tag{3.5}$$

Note that we do not enforce $\mathbf{F} = \mathbf{f}(\mathbf{W}^{H_3}, \widetilde{\mathbf{B}}_M)$. The reason is that we allow π_1 of (2.7) to be a free variable, hence taking the role of the relaxation pressure in [7]. For consistency we have to set $\pi_1 = p + \frac{B_2^2+B_3^2}{2} + B_2\widetilde{B}_2 + B_3\widetilde{B}_3$ in $\mathbf{F}_L$ and $\mathbf{F}_R$. The outer wave speeds s_L and s_R model the fast magneto-sonic waves and are defined as in [14,22], i.e.,

$$s_L = \min\{u_{1L} - c_{fL}, \bar{u}_1 - \bar{c}_f\}, \quad s_R = \max\{u_{1R} + c_{fR}, \bar{u}_1 + \bar{c}_f\}, \tag{3.6}$$

where $\bar{u}_1$ and $\bar{c}_f$ are the normal velocity and the fast wave speed of the Jacobian matrix $A((\mathbf{W}_L + \mathbf{W}_R)/2)$ respectively. This choice is important for numerical stability and accuracy.

In order to describe the solver, we need to determine the speed of the middle wave s_M and the intermediate states $\mathbf{W}_L^*, \mathbf{W}_R^*$. The middle wave models a material contact discontinuity. Hence, the velocity field and the tangential magnetic fields are assumed to be constant across the middle wave. This allows us to define $\mathbf{u}^* = \mathbf{u}_L^* = \mathbf{u}_R^*$, $B_2^* = B_{2L}^* = B_{2R}^*$ and $B_3^* = B_{3L}^* = B_{3R}^*$. As in [19], the normal magnetic field B_1 is not assumed to be constant but jumps only across the middle wave (modeling the linear degenerate "divergence wave" implied by (2.2)), and B_1 is constant across the outer waves. The only difference between the solver designed here and the three wave solver described in [19] is the fact that we include a parameter $\widetilde{\mathbf{B}}_M$ in our expressions and we must account for it in the conservation relations below.

We impose local conservation across each wave to determine the various states. Local conservation across the outermost waves means that

$$s_L\mathbf{W}_L^* - \mathbf{F}_L^* = s_L\mathbf{W}_L - \mathbf{F}_L, \quad \text{and} \quad s_R\mathbf{W}_R - \mathbf{F}_R = s_R\mathbf{W}_R^* - \mathbf{F}_R^*. \tag{3.7}$$

Conservation across the middle wave s_M involves taking the source term $\mathbf{s}^1$ in (3.2) into account. The conservation relation reads

$$s_M\mathbf{W}_R^* - s_M\mathbf{W}_L^* = \mathbf{F}_R^* - \mathbf{F}_L^* + \mathbf{s}^{1,*}, \tag{3.8}$$

where

$$\mathbf{s}^{1,*} = \begin{pmatrix} 0 \\ -\frac{B_{1R}^2 - B_{1L}^2}{2} - \widetilde{B}_{1M}(B_{1R} - B_{1L}) \\ -\left(B_2^* + \widetilde{B}_{2M}\right)(B_{1R} - B_{1L}) \\ -\left(B_3^* + \widetilde{B}_{3M}\right)(B_{1R} - B_{1L}) \\ -\mathbf{u}^*(B_{1R} - B_{1L}) \\ -u_1^*\frac{B_{1R}^2 - B_{1L}^2}{2} - \left(u_2^*B_2^* + u_3^*B_3^*\right)(B_{1R} - B_{1L}) \end{pmatrix}. \tag{3.9}$$

This amounts to integrating the source $\mathbf{s}^1$ in (3.2) across the wave fan as described in the next section. The above expression follows from the assumption that B_1 jumps only across the middle wave while the velocity field and the tangential components of the magnetic field remain constant.

For any middle speed s_M, a straightforward application of the conservation relations (3.7) determines unique values of ρ_θ^* given by

$$\rho_\theta^* = \rho_\theta \frac{u_{1\theta} - s_\theta}{s_M - s_\theta}, \quad \theta \in \{L, R\}. \tag{3.10}$$

Using conservation across all the three waves (adding (3.7) and (3.8)) results in the global conservation relation,

$$\mathbf{F}_R - \mathbf{F}_L = s_R\mathbf{W}_R - s_L\mathbf{W}_L + (s_M - s_R)\mathbf{W}_R^* + (s_L - s_M)\mathbf{W}_L^* + \mathbf{s}^{1,*}. \tag{3.11}$$

We can use the intermediate density states (3.10) and global conservation (3.11) to obtain

$$s_M = u_1^* = \frac{\pi_{1R} - \pi_{1L} + \rho_R u_{1R}(u_{1R} - s_R) - \rho_L u_{1L}(u_{1L} - s_L)}{\rho_R(u_{1R} - s_R) - \rho_L(u_{1L} - s_L)}.$$

Similarly, one uses local conservation (3.7) across the two outer waves to obtain the intermediate "relaxed" pressures,

$$\pi_{1\theta}^* = \pi_{1\theta} + \rho_\theta(u_{1\theta} - s_\theta)(u_{1\theta} - s_M), \tag{3.12}$$

for $\theta \in \{L, R\}$. Note that conservation across the middle wave automatically implies that $\pi_{1L}^* = \pi_{1R}^*$, and that (3.12) confirms this assertion. The next step is to determine the tangential velocity and magnetic field. Using global conservation across the wave fan (3.11), we obtain that the intermediate values u_σ^* and B_σ^* satisfy the following two linear equations,

$$\alpha u_\sigma^* - \beta B_\sigma^* = c_\sigma, \quad -\beta u_\sigma^* - \zeta B_\sigma^* = d_\sigma, \quad \sigma \in \{2, 3\},$$

where

$$\begin{aligned}
c_\sigma &= \rho_R u_{\sigma R}(u_{1R}-s_R) - \rho_L u_{\sigma L}(u_{1L}-s_L)\\
&\quad -(B_{1R}B_{\sigma R}-B_{1L}B_{\sigma L}) - \widetilde{B}_{1M}(B_{\sigma R}-B_{\sigma L}),\\
d_\sigma &= B_{\sigma R}(u_{1R}-s_R) - B_{\sigma L}(u_{1L}-s_L)\\
&\quad -(B_{1L}u_{\sigma L}-B_{1R}u_{\sigma R}) + \widetilde{B}_{\sigma M}(u_{1R}-u_{1L}) - \widetilde{B}_1(u_{\sigma R}-u_{\sigma L}),\\
\alpha &= \rho_R(u_{1R}-s_R) - \rho_L(u_{1L}-s_L),\\
\zeta &= s_R - s_L,\\
\beta &= B_{1R}-B_{1L}.
\end{aligned} \tag{3.13}$$

Solving the linear system (3.13), the intermediate tangential components of velocity and magnetic field are obtained as

$$u^*_\sigma = \frac{\zeta c_\sigma - \beta d_\sigma}{\alpha\zeta+\beta^2}, \quad B^*_\sigma = \frac{-\alpha d_\sigma - \beta c_\sigma}{\alpha\zeta+\beta^2}. \tag{3.14}$$

Remark 3.1. In general, the denominator; $\alpha\zeta+\beta^2$, in (3.14) can become small, leading to a degeneracy in the states. A simple calculation shows that $\alpha\zeta+\beta^2\neq 0$ if $\left(\rho_R c_f^R + \rho_L c_f^L\right)(s_R-s_L) > (B_{1R}-B_{1L})^2$. This condition can be ensured by modifying the wave speeds (3.6) to $s_L = \min(\tilde{s}_L, \bar{u}_1 - \bar{c}_f)$ and $s_R = \max(\tilde{s}_R, \bar{u}_1 + \bar{c}_f)$ where the new element is the slightly 'faster' fast wave speeds

$$\tilde{s}_R = u_{1R} + \frac{1}{2}(\max((u_{1L}-u_{1R}),0)) + \tilde{c}_{fR}, \quad \tilde{s}_L = u_{1L} - \frac{1}{2}(\max((u_{1L}-u_{1R}),0)) - \tilde{c}_{fL}, \tag{3.15}$$

with

$$\tilde{c}^2_{f\theta} = \frac{\gamma p_\theta}{\rho_\theta} + \frac{\overline{B}^2_{1\theta}}{\rho_\theta}(1+\epsilon) + \frac{\overline{B}^2_{2\theta}+\overline{B}^2_{3\theta}}{\rho_\theta} + \sqrt{\left(\frac{\gamma p_\theta + |\overline{\mathbf{B}}|^2_\theta}{\rho_\theta}\right)^2 - 4\frac{\gamma p_\theta \overline{B}^2_{1\theta}}{\rho^2_\theta}}, \quad \theta\in\{L,R\}.$$

Here, ϵ is a small positive constant, and $\overline{B}_{\sigma\theta} = B_{\sigma\theta} + \widetilde{B}_{\sigma M}$ with $\sigma\in\{1,2,3\}$. This slight 'widening' of the wave fan ensures that the denominator $\alpha\zeta+\beta^2$ is never zero, and hence that the intermediate states are well defined. Details of this modification can be checked from [19].

Finally, the intermediate total energy states are determined by local conservation relations (3.7)

$$E^*_\theta = \frac{1}{s_M - s_\theta}\left(E_\theta(u_{1\theta}-s_\theta) + \pi_{1\theta}u_{1\theta} - \pi^*_{1\theta}s_M + \frac{B^2_{1\theta}}{2}(u_{1\theta}-s_M) + (B_{1\theta}+\widetilde{B}_{1M})\left(B_{2\theta}u_{2\theta} + B_{3\theta}u_{3\theta} - B^*_{2\theta}u^*_{2\theta} - B^*_{3\theta}u^*_{3\theta}\right)\right),$$

for $\theta\in\{L,R\}$. Hence, all the intermediate states are determined explicitly. The intermediate fluxes are obtained in terms of the intermediate states by local conservation (3.7),

$$\mathbf{F}^*_L = \mathbf{F}_L + s_L(\mathbf{W}^*_L - \mathbf{W}_L), \quad \mathbf{F}^*_R = \mathbf{F}_R + s_R(\mathbf{W}^*_R - \mathbf{W}_R).$$

Combining the above expressions for the states and the fluxes, we write down our explicit flux formula for the three-wave solver as

$$\mathbf{F}^{H_3}_{i+1/2,j} = \begin{cases} \mathbf{F}_{i,j} & ,\text{if } s_{L,i+1/2,j} > 0,\\ \mathbf{F}^*_{i,j} & ,\text{if } s_{L,i+1/2,j} \leqslant 0 \wedge s_{M,i+1/2,j} \geqslant 0,\\ \mathbf{F}^*_{i+1,j} & ,\text{if } s_{M,i+1/2,j} < 0 \wedge s_{R,i+1/2,j} \geqslant 0,\\ \mathbf{F}_{i+1,j} & ,\text{if } s_{R,i+1/2,j} < 0. \end{cases} \tag{3.16}$$

Note that this may be discontinuous at $s_{M,i+1/2,j} = 0$ according to (3.8). Hence our choice of $\mathbf{F}^{H_3}$ in that case is merely a convention. It is the proper addition of the source term which ensures that the scheme is continuous.

3.1.3. Discretization of the Godunov–Powell source term

In this section we motivate (3.8), and specify the discrete source $\mathbf{S}^{1,n}_{i,j}$ in (3.1). The discrete source must be consistent with the Godunov–Powell source term in the x-direction $\mathbf{s}^1(\mathbf{W}, \widetilde{\mathbf{B}}, \mathbf{W}_x)$. It will be determined from our solution of the Riemann problem (3.2) along the x-direction at the cell interfaces $(x_{i+1/2}, y_j)$. The HLL three wave approximate Riemann solver of the previous section provide us with the assumptions we need: The normal magnetic field jumps only across the contact discontinuity modeled by the middle wave, while the velocity field and the tangential components of the magnetic field are constant across the middle wave.

We follow the presentation in [19] and let T be a quantity that is constant with value T^* across the middle wave, then

$$\left(TB^1_x\right)(x,t) = T^*(B_{1R}-B_{1L})\delta(x+tu^*_1), \tag{3.17}$$

where δ denotes the Dirac delta function. If we assume that $|u^*_1|\Delta t^n \leqslant \Delta x$, integrating TB^1_x over $(0,\Delta t^n)\times(-\Delta x, 0)$ yields

$$\frac{1}{\Delta x}\int_0^{\Delta t^n}\int_{-\Delta x}^{0} TB_x^1\,dx\,dt = \Delta t^n T^* \frac{B_{1R}-B_{1L}}{\Delta x}\mathbf{1}_{\{u_1^*<0\}}, \tag{3.18}$$

where $\mathbf{1}_A$ denotes the characteristic function of the set A. Integration over $(0,\Delta t^n)\times(0,\Delta x)$ leads to

$$\frac{1}{\Delta x}\int_0^{\Delta t^n}\int_{0}^{\Delta x} TB_x^1\,dx\,dt = \Delta t^n T^* \frac{B_{1R}-B_{1L}}{\Delta x}\mathbf{1}_{\{u_1^*>0\}},$$

under the same restriction, $|u_1^*|\Delta t^n \leqslant \Delta x$. Similarly, by again using the assumption that B_1 jumps only across the contact discontinuity and T remains constant across it, we obtain that

$$\frac{1}{\Delta x}\int_0^{\Delta t^n}\int_{-\Delta x}^{0} T\left(\frac{B_1^2}{2}\right)_x dx\,dt = \Delta t^n T^* \frac{B_{1R}^2-B_{1L}^2}{2\Delta x}\mathbf{1}_{\{u_1^*<0\}},$$

and

$$\frac{1}{\Delta x}\int_0^{\Delta t^n}\int_{0}^{\Delta x} T\left(\frac{B_1^2}{2}\right)_x dx\,dt = \Delta t^n T^* \frac{B_{1R}^2-B_{1L}^2}{2\Delta x}\mathbf{1}_{\{u_1^*>0\}}. \tag{3.19}$$

Hence, we can derive (3.8) from (3.18) and (3.19) by observing that we must have

$$\mathbf{s}^{1,*} = \int_{t^n}^{t^{n+1}}\int_{-\Delta x}^{\Delta x} \mathbf{s}^1\left(\mathbf{W}^{H_3}, \widetilde{\mathbf{B}}_M, \mathbf{W}_x^{H_3}\right)dx\,dt.$$

The final scheme is defined by evolving the piecewise constant function $\mathbf{W}_{i,j}$ according to the approximate Riemann solver (3.5), and then taking the cell average of the conserved quantities. Hence, the scheme is determined by (3.7) and (3.8), yielding (3.16), and

$$\mathbf{S}_{i,j}^{1,n} = \mathbf{s}_{i-1/2,j}^{1,*}\mathbf{1}_{\{(s_{M,i-1/2,j}\geqslant 0)\}} + \mathbf{s}_{i+1/2,j}^{1,*}\mathbf{1}_{\{(s_{M,i+1/2,j}<0)\}}, \tag{3.20}$$

where $\mathbf{s}_{i\pm1/2,j}^{1,*}$ is defined in (3.9). For the case $s_{M,i+1/2,j}=0$, our choice in (3.20) was dictated by our choice in (3.16). Integration along the y-direction is taken care of by the midpoint rule.

We emphasize that the discrete Godunov–Powell source term in each cell consists of contributions from Riemann solutions at the bordering interfaces and depends on the sign of the middle wave at each interface. Thus, the Godunov–Powell source term is suitably upwinded. Note that assuming the normal magnetic field B_1 to be constant for the whole domain leads to the source term being zero. This approach follows [19,7] and is very different from the usual centered discretization of the Godunov–Powell source term ([40] and references therein).

Thus, we have completed the descriptions of the numerical fluxes $\mathbf{F}$ and the source $\mathbf{S}^1$ in (3.1).

Remark 3.2. The above fluxes and sources are designed using a three wave solver. An alternative would be to design a five wave solver like in [36,19]. This solver models Alfvén waves in addition to the outer most fast waves and the contact discontinuity. We can follow the steps of [18] to design a five wave solver for (3.2) by taking into account contributions of the parameter $\widetilde{\mathbf{B}}$.

3.1.4. Fluxes and sources in the y-direction

The numerical flux $\mathbf{G}$ and discrete Godunov–Powell source term $\mathbf{S}^2$ in (3.1) are similarly described in terms of the following Riemann problem

$$\mathbf{W}_t + \mathbf{g}(\mathbf{W}, \widetilde{\mathbf{B}}_m)_y = \mathbf{s}^2(\mathbf{W}, \widetilde{\mathbf{B}}_m, \mathbf{W}_y), \quad \mathbf{W}(y,0) = \begin{cases}\mathbf{W}_B & y<0,\\ \mathbf{W}_T & y>0,\end{cases} \tag{3.21}$$

where $\mathbf{g}$ and $\mathbf{s}^2$ are defined in (2.6) and (2.8) respectively. The natural way to specify initial data $\mathbf{W}_{T,B}$ in the above problem is to use the states $\mathbf{W}_B = \mathbf{W}_{i,j}^n$ and $\mathbf{W}_T = \mathbf{W}_{i,j+1}^n$. However, this approach leads to a scheme that does not preserve discrete versions of the interesting steady states (2.11). Therefore we must design suitable fluxes in order to design well-balanced schemes.

3.1.5. Local hydrostatic reconstructions

Instead of just using the cell averages below and above the interface as data in (3.21), we utilize the special structure of the isothermal steady states (2.11) and perform a local hydrostatic reconstruction inside the cell, i.e., we observe that the pressure and density at steady state (2.11) have an exponentially decaying profile. We use the same structure locally inside a cell to define

$$\mathbf{V}_B = \left\{\rho_{i,j+1/2}^{n,-}, \mathbf{u}_{i,j}^n, \mathbf{B}_{i,j}^n, p_{i,j+1/2}^{n,-}\right\}, \quad \mathbf{V}_T = \left\{\rho_{i,j+1/2}^{n,+}, \mathbf{u}_{i,j+1}^n, \mathbf{B}_{i,j+1}^n, p_{i,j+1/2}^{n,+}\right\}, \tag{3.22}$$

where the reconstructed density and pressure are given in terms of extrapolated cell averages by

$$\begin{aligned}
\rho^{n,-}_{i,j+1/2} &= \rho^n_{i,j} e^{\frac{-\Delta y}{2H^n_{i,j}}}, \quad p^{n,-}_{i,j+1/2} = p^n_{i,j} e^{\frac{-\Delta y}{2H^n_{i,j}}}, \\
\rho^{n,+}_{i,j+1/2} &= \rho^n_{i,j+1} e^{\frac{\Delta y}{2H^n_{i,j+1}}}, \quad p^{n,+}_{i,j+1/2} = p^n_{i,j} e^{\frac{\Delta y}{2H^n_{i,j+1}}},
\end{aligned} \tag{3.23}$$

with the local scale height $H^n_{i,j} = \frac{p^n_{i,j}}{g\rho^n_{i,j}}$. The above sub-cell hydrostatic reconstruction has been inspired by the approach of [1] to design well-balanced schemes for the shallow water equations with bottom topography. It involves using the steady state density and pressure (2.11) to define the reconstructed densities and pressures at the cell edges in the y-direction.

The data $\mathbf{W}_B$ and $\mathbf{W}_T$ (in terms of conservative variables) are easily obtained from the primitive variables $\mathbf{V}_B, \mathbf{V}_T$. The parameter $\widetilde{\mathbf{B}}_m$ in (3.21) is given by the average,

$$\widetilde{\mathbf{B}}_m = \widetilde{\mathbf{B}}_{i,j+1/2} = \frac{\widetilde{\mathbf{B}}_{i,j} + \widetilde{\mathbf{B}}_{i,j+1}}{2}. \tag{3.24}$$

Hence, we stagger the parameter $\widetilde{\mathbf{B}}$ in defining the approximate Riemann solver as in the previous section.

An approximate Riemann solution of the problem (3.2) in terms of the HLL three wave solver of the previous section is easily obtained by repeating the approach of describing the solver in the x-direction. This can be used to describe the flux $\mathbf{G}$ and source $\mathbf{S}^2$. Note that the difference between the design of the fluxes and Godunov–Powell sources in the x and the y-directions is due to the use of local hydrostatic reconstructions of the density and the pressure in the y-direction.

3.1.6. Discretization of the gravitational source term

We need to discretize the gravity source term to define $\mathbf{S}^g$ in (3.1). Instead of using a simple evaluation of the gravity term (it does not involve any derivatives) inside each cell, we follow an approach suggested in [1] for shallow water equations with topography to define

$$\mathbf{S}^{g,n}_{i,j} = \left\{0, 0, \frac{p^{n,-}_{i,j+1/2} - p^{n,+}_{i,j-1/2}}{\Delta y}, 0, 0, 0, 0, -\rho^n_{i,j} u^n_{2,i,j} g\right\}. \tag{3.25}$$

where $p^{n,-}_{i,j+1/2}, p^{n,+}_{i,j-1/2}$ are defined in (3.23). We will prove that this discretization of the gravity source term is consistent, and that it ensures well-balancing of the scheme.

3.1.7. Boundary conditions

In order to complete our description of the scheme (3.1), we need to specify boundary conditions in both directions. As mentioned before, we use periodic boundary conditions in the horizontal x-direction by setting,

$$\mathbf{W}^n_{0,j} = \mathbf{W}^n_{N_x,j}, \quad \mathbf{W}^n_{N_x+1,j} = \mathbf{W}^n_{1,j}. \tag{3.26}$$

In the vertical y-direction, we use the following balanced Neumann type boundary conditions,

$$\begin{aligned}
\mathbf{B}^n_{i,0} &= \mathbf{B}^n_{i,1}, \qquad \mathbf{B}^n_{i,N_y+1} = \mathbf{B}^n_{i,N_y}, \\
\mathbf{w}^n_{i,0} &= \mathbf{w}^n_{i,1} e^{\frac{\Delta y}{H_i}}, \quad \mathbf{w}^n_{i,N_y+1} = \mathbf{w}^n_{i,N_y} e^{-\frac{\Delta y}{H_i}},
\end{aligned} \tag{3.27}$$

where $\mathbf{w}$ denotes the 5-vector $\{\rho, \rho\mathbf{u}, p\}$. This completes the description of the first-order scheme (3.1). Some properties of this scheme are summarized in the theorem below,

Theorem 1. *Consider the scheme (3.1) approximating the system (2.5). This scheme has the following properties,*

(i) The scheme (3.1) is consistent with (2.4), and it is first-order accurate in both space and time (for smooth solutions).
(ii) The scheme (3.1) is well-balanced and preserves discrete versions of the steady state (2.11), i.e., given data satisfying

$$\mathbf{u}^n_{i,j} = 0, \quad \mathbf{B}^n_{i,j} = 0, \quad \rho^n_{i,j} = \rho^0_{i,j} e^{\frac{-y_j}{H}}, \quad p^n_{i,j} = p^0_{i,j} e^{\frac{-y_j}{H}}, \tag{3.28}$$

and any background field $\widetilde{\mathbf{B}}$, then the numerical update $\mathbf{W}^{n+1}_{i,j}$ is

$$\mathbf{W}^{n+1}_{i,j} \equiv \mathbf{W}^n_{i,j}.$$

Proof. We start by proving consistency of (3.1). The flux $\mathbf{F}$ and discrete source $\mathbf{S}^1$ are clearly consistent. Observe from (3.23) that $(\rho^{n,\pm}_{i,j+1/2}, p^{n,\pm}_{i,j+1/2}) \to (\rho^n_{i,j}, p^n_{i,j})$ as $\Delta y \to 0$. Hence, $\mathbf{G}$ and $\mathbf{S}^2$ are also clearly consistent. The consistency of the gravitational source term $\mathbf{S}^g$ in (3.25) is a consequence of the following elementary identity,

$$\frac{p^{n,-}_{i,j+1/2} - p^{n,+}_{i,j-1/2}}{\Delta y} = -g\rho^n_{i,j} \frac{e^{\frac{\Delta y}{2H^n_{i,j}}} - e^{\frac{-\Delta y}{2H^n_{i,j}}}}{\frac{\Delta y}{H^n_{i,j}}} = -g\rho^n_{i,j} + O(\Delta y^2). \tag{3.29}$$

In fact, (3.29) shows that the gravity source term $\mathbf{S}^g$ in (3.25) is in fact second-order accurate. The first-order accuracy of (3.1) is very easy to check.

To prove that scheme (3.1) is well-balanced, we observe that the data (3.28) are constant in the x-direction. Therefore, the flux differences $F^n_{i+1/2,j} - F^n_{i-1/2,j}$ are zero for $1 \leqslant i \leqslant N_x$ and for all j (including the boundaries). The source terms $\mathbf{S}^1$ and $\mathbf{S}^2$ are zero because $\mathbf{B}^n_{i,j} = 0$ for all i,j (including the boundaries).

Insert the data (3.28) into (3.23) and we obtain,

$$\rho^{n,-}_{ij+1/2} = \rho^n_{ij} e^{\frac{-\Delta y}{2H}} = \rho^0_{ij} e^{\frac{-y_j}{H}} e^{\frac{-\Delta y}{2H}} = \rho^0_{ij} e^{\frac{-y_j}{H}} e^{\frac{-\Delta y}{H}} e^{\frac{\Delta y}{2H}} = \rho^n_{ij+1} e^{\frac{\Delta y}{2H}} = \rho^{n,+}_{ij+1/2}.$$

A similar calculation holds for the pressure. Consequently for all i,j (including the boundaries),

$$\begin{aligned} &\rho^{n,-}_{ij+1/2} = \rho^{n,+}_{ij+1/2}, \quad \mathbf{u}^n_{ij} = \mathbf{u}^n_{ij+1} = 0 \\ &p^{n,-}_{ij+1/2} = p^{n,+}_{ij+1/2}, \quad \mathbf{B}^n_{ij} = \mathbf{B}^n_{ij+1} = 0. \end{aligned} \tag{3.30}$$

Hence the numerical flux $\mathbf{G}$ is

$$\mathbf{G}^n_{ij+1/2} = \mathbf{g}\Big(\rho^n_{ij+1/2}, 0, 0, p^n_{ij+1/2}, \rho^n_{ij+1/2}, 0, 0, p^n_{ij+1/2}, \widetilde{\mathbf{B}}_{ij+1/2}\Big)$$

and by consistency of the flux in (2.6), we have

$$\mathbf{G}^n_{ij+1/2} = \mathbf{G}\Big(\rho^n_{ij+1/2}, 0, 0, p^n_{ij+1/2}, \tilde{\mathbf{B}}_{ij+1/2}\Big) = (0, 0, p_{ij+1/2}, 0, 0, 0, 0, 0). \tag{3.31}$$

Similarly an explicit evaluation of the gravity source term (3.25) yields,

$$\mathbf{S}^{g,n}_{ij} = \left\{0, 0, \frac{p^n_{ij+1/2} - p^n_{ij-1/2}}{\Delta y}, 0, 0, 0, 0, 0\right\}.$$

Therefore combining the above two expressions, we obtain

$$\frac{\mathbf{G}^n_{ij+1/2} - \mathbf{G}^n_{ij,-1/2}}{\Delta y} = \mathbf{S}^{n,g}_{ij} \quad \text{for all } i \text{ and } j.$$

Using the above identity in (3.1) and the fact that flux differences in the x-direction and the Godunov–Powell source terms vanish leads to

$$\mathbf{W}^{n+1}_{ij} \equiv \mathbf{W}^n_{ij}.$$

Hence, the scheme (3.1) is well-balanced with respect to the discrete steady state (3.28). □

Remark 3.3. It is important that the scheme produces positive states, i.e., states with positive values of density and pressure. For zero gravity and a constant $\widetilde{\mathbf{B}}$, the positivity conditions of [53] (see also [4]) apply. They amount to ensuring that the state $3\mathbf{W}^n_{ij} - \mathbf{W}^{n,-}_{ij+1/2} - \mathbf{W}^{n,+}_{ij-1/2}$ is positive. In our case this means that $3 - 2\cosh(\Delta y/(2H_{ij})) > 0$, which holds as long as the local scale height H_{ij} is reasonably resolved. For nonconstant $\widetilde{\mathbf{B}}$ the techniques of [53] do not apply, and no proof of positivity is known. Finally, when gravity is added, density trivially remains positive, while we expect pressure to remain positive at resolved scale heights.

3.2. The second-order scheme

The finite volume scheme (3.1) is first-order accurate in both space and time. For practical applications, we need higher order of accuracy. We will design a finite volume scheme based on (3.1) which is second-order accurate in both space and time. At any time t, given the cell averages $\mathbf{W}_{ij}(t)$, the semi-discrete form of this scheme is given by

$$\frac{d}{dt}\mathbf{W}_{ij} = \mathcal{F}_{ij} = -\frac{1}{\Delta x}(\widetilde{\mathbf{F}}_{i+1/2,j} - \widetilde{\mathbf{F}}_{i-1/2,j}) - \frac{1}{\Delta y}(\widetilde{\mathbf{G}}_{ij+1/2} - \widetilde{\mathbf{G}}_{ij-1/2}) + \widetilde{\mathbf{S}}^1_{ij} + \widetilde{\mathbf{S}}^2_{ij} + \mathbf{S}^g_{ij}. \tag{3.32}$$

The numerical fluxes $\mathbf{F}, \mathbf{G}$ and the sources $\widetilde{\mathbf{S}}^1, \widetilde{\mathbf{S}}^2$ are defined below.

It is standard (see [29]) to replace the piecewise constant approximation $\mathbf{W}_{ij}$ with a non-oscillatory piecewise linear reconstruction in order to obtain second-order spatial accuracy. There are a variety of reconstructions including the popular TVD-MUSCL limiters [52], ENO reconstruction [24] and WENO reconstruction [45]. The ENO and WENO reconstructions can be extended to even higher orders of accuracy.

A standard reconstruction is performed in terms of the conservative variables $\mathbf{W}$. However, such a reconstruction may not preserve discrete steady states like (2.11). Hence, we introduce a novel reconstruction procedure (see [1,37] for well-balanced reconstructions of shallow water equations with topography) based on the following *equilibrium* variables,

$$\mathbf{R}_{ij} = \{\mathbf{L}\rho_{ij}, \mathbf{u}_{ij}, \mathbf{B}_{ij}, \mathbf{L}p_{ij}\}, \tag{3.33}$$

where

$$\mathbf{L}\rho_{i,j} = \log(\rho_{i,j}), \quad \mathbf{L}p_{i,j} = \log(p_{i,j}).$$

Next, we use the equilibrium variables in each cell to define non-oscillatory slopes inside each cell by the following procedures.

3.2.1. Minmod reconstruction (MM)

Given the cell averages $\mathbf{W}_{i,j}$, we calculate the equilibrium variables $\mathbf{R}_{i,j}$ defined in (3.33). Define the Minmod-differences in each direction as

$$\begin{aligned} D^x\mathbf{R}_{i,j} &= \operatorname{minmod}(\mathbf{R}_{i+1,j} - \mathbf{R}_{i,j}, \mathbf{R}_{i,j} - \mathbf{R}_{i-1,j}), \\ D^y\mathbf{R}_{i,j} &= \operatorname{minmod}(\mathbf{R}_{i,j+1} - \mathbf{R}_{i,j}, \mathbf{R}_{i,j} - \mathbf{R}_{i,j-1}) \end{aligned} \tag{3.34}$$

where

$$\operatorname{minmod}(a,b) = \frac{1}{2}(\operatorname{sgn}(a) + \operatorname{sgn}(b)) \min(|a|, |b|).$$

Note that the limiting is performed componentwise.

3.2.2. ENO reconstruction

Given the cell averages $\mathbf{W}_{i,j}$, calculate the equilibrium variables $\mathbf{R}_{i,j}$ by (3.33). Define the ENO-differences in each direction as

$$D^x\mathbf{R}_{i,j} = \begin{cases} \mathbf{R}_{i+1,j} - \mathbf{R}_{i,j} & \text{if } \Gamma^x_{i,j} \leqslant 1, \\ \mathbf{R}_{i,j} - \mathbf{R}_{i-1,j} & \text{otherwise}, \end{cases} \quad D^y\mathbf{R}_{i,j} = \begin{cases} \mathbf{R}_{i,j+1} - \mathbf{R}_{i,j} & \text{if } \Gamma^y_{i,j} \leqslant 1, \\ \mathbf{R}_{i,j} - \mathbf{R}_{i,j-1} & \text{otherwise}, \end{cases} \tag{3.35}$$

where

$$\Gamma^x_{i,j} = \frac{|\psi(\mathbf{V}_{i+1,j}) - \psi(\mathbf{V}_{i,j})|}{|\psi(\mathbf{V}_{i,j}) - \psi(\mathbf{V}_{i-1,j})|}, \quad \Gamma^y_{i,j} = \frac{|\psi(\mathbf{V}_{i,j+1}) - \psi(\mathbf{V}_{i,j})|}{|\psi(\mathbf{V}_{i,j}) - \psi(\mathbf{V}_{i,j-1})|},$$

for some function ψ called the global smoothness indicator. Here $\mathbf{V}$ denotes the primitive variables $\mathbf{V}_{i,j} = \{\rho_{i,j}, \mathbf{u}_{i,j}, \mathbf{B}_{i,j}, p_{i,j}\}$. We use $\psi(\mathbf{V}) = \rho + \mathbf{B}^2$. This choice of ψ is just one possibility and other choices can be made. However, this choice is quite robust in practice (see [19]). Note that for a piecewise linear reconstruction, the ENO procedure reduces to providing a limiter for the slopes in each direction.

3.2.3. WENO procedure

As an alternative to the above reconstruction, consider the following cell-differences

$$\begin{aligned} D^x\mathbf{R}_{i,j} &= \left(\omega^x_{i,j}(\mathbf{R}_{i+1,j} - \mathbf{R}_{i,j}) + \left(1 - \omega^x_{i,j}\right)(\mathbf{R}_{i,j} - \mathbf{R}_{i-1,j})\right), \\ D^y\mathbf{R}_{i,j} &= \left(\omega^y_{i,j}(\mathbf{R}_{i,j+1} - \mathbf{R}_{i,j}) + \left(1 - \omega^y_{i,j}\right)(\mathbf{R}_{i,j} - \mathbf{R}_{i,j-1})\right), \end{aligned} \tag{3.36}$$

where the weights are given by,

$$\begin{aligned} \omega^x_{i,j} &= \frac{a^0_{i,j}}{a^0_{i,j} + a^1_{i,j}}, \quad a^0_{i,j} = \frac{1}{3\left(\epsilon + \beta^{x,0}_{i,j}\right)}, \quad a^1_{i,j} = \frac{2}{3\left(\epsilon + \beta^{x,1}_{i,j}\right)}, \\ \omega^y_{i,j} &= \frac{b^0_{i,j}}{b^0_{i,j} + b^1_{i,j}}, \quad b^0_{i,j} = \frac{1}{3\left(\epsilon + \beta^{y,0}_{i,j}\right)}, \quad b^1_{i,j} = \frac{2}{3\left(\epsilon + \beta^{y,1}_{i,j}\right)}, \end{aligned}$$

where ϵ is a small positive number, and the parameters are given by

$$\begin{aligned} \beta^{x,0}_{i,j} &= (\psi(\mathbf{V}_{i+1,j}) - \psi(\mathbf{V}_{i,j}))^2, \quad \beta^{x,1} = (\psi(\mathbf{V}_{i,j}) - \psi(\mathbf{V}_{i-1,j}))^2, \\ \beta^{y,0}_{i,j} &= (\psi(\mathbf{V}_{i,j+1}) - \psi(\mathbf{V}_{i,j}))^2, \quad \beta^{y,1} = (\psi(\mathbf{V}_{i,j}) - \psi(\mathbf{V}_{i,j-1}))^2, \end{aligned}$$

and the indicator function ψ is defined above. The WENO reconstruction leads to a third-order accurate approximation.

Remark 3.4. The above procedures do not necessarily lead to schemes that preserve positive pressure. A provably positive scheme, at least for constant $\widetilde{\mathbf{B}}$, can be obtained with the framework outlined in recent papers [53,19] with suitable modifications. We did not observe problems with positivity in our numerical simulations in this paper. One stabilizing factor was the use of logarithms of the pressure and density in the reconstruction, which automatically ensures positivity of the reconstructed pressure and density. Hence, we omit details of positivity preserving modifications here and refer the reader to [19,53] for details.

All the above procedures supply slopes $D^x\mathbf{R}_{i,j}$ and $D^y\mathbf{R}_{i,j}$ and can be used to define the following reconstructed piecewise linear function is each cell $I_{i,j}$ denoted by

$$\overline{\mathbf{R}}_{i,j}(x,y) = \mathbf{R}_{i,j} + \frac{1}{\Delta x} D^x \mathbf{R}_{i,j}(x - x_i) + \frac{1}{\Delta y} D^y \mathbf{R}_{i,j}(y - y_j). \tag{3.37}$$

where the gradients $D^{x,y}$ may be defined by the minmod (3.34), ENO (3.35) or WENO (3.36) procedures. The reconstructed primitive variables are obtained from the reconstructed equilibrium variables by the following simple transformation,

$$\mathbf{V}_{i,j}(x,y) = \{e^{\mathbf{L}\rho_{i,j}(x,y)}, \mathbf{u}_{i,j}(x,y), \mathbf{B}_{i,j}(x,y), e^{\mathbf{L}p_{i,j}(x,y)}\}.$$

Hence, the reconstruction procedure outlined here entails taking a logarithm of the pressure and density, reconstruct in these variables and transforming back via an exponential to obtain the reconstructed primitive variables. The conservative variables can be trivially obtained from the primitive variables and are denoted by the piecewise linear function $\mathbf{W}_{i,j}(x,y)$.

Define the point values,

$$\mathbf{W}^E_{i,j} = \mathbf{W}_{i,j}(x_{i+1/2}, y_j), \quad \mathbf{W}^W_{i,j} = \mathbf{W}_{i,j}(x_{i-1/2}, y_j),$$
$$\mathbf{W}^N_{i,j} = \mathbf{W}_{i,j}(x_i, y_{j+1/2}), \quad \mathbf{W}^S_{i,j} = \mathbf{W}_{i,j}(x_i, y_{j+1/2}).$$

We use these point values to define the numerical fluxes by

$$\widetilde{\mathbf{F}}_{i+1/2,j} = \mathbf{F}\Big(\mathbf{W}^E_{i,j}, \mathbf{W}^W_{i+1,j}, \widetilde{\mathbf{B}}_{i+1/2,j}\Big), \quad \widetilde{\mathbf{G}}_{i,j+1/2} = \mathbf{G}\Big(\mathbf{W}^N_{i,j}, \mathbf{W}^S_{i,j+1}, \widetilde{\mathbf{B}}_{i,j+1/2}\Big),$$

where $\mathbf{F}$ and $\mathbf{G}$ are given by the three wave solver of the previous section. The value of the staggered parameter $\widetilde{\mathbf{B}}$ is given by a simple evaluation,

$$\widetilde{\mathbf{B}}_{i+1/2,j} = \widetilde{\mathbf{B}}(x_{i+1/2}, y_j), \quad \widetilde{\mathbf{B}}_{i,j+1/2} = \widetilde{\mathbf{B}}(x_i, y_{j+1/2}).$$

The above choice ensures second-order accuracy for smooth (say C^2) parameters $\widetilde{\mathbf{B}}$. In case the parameter is not smooth enough, or given by cell averages, we can reconstruct the parameter on a staggered mesh. A crucial difference between the first-order and the second-order fluxes is the definition of $\mathbf{G}$. In the first-order scheme, hydrostatic reconstructions (3.23) were used to define the flux in the y-direction. The piecewise linear reconstruction in terms of the equilibrium variables (3.33) automatically ensures local hydrostatic balance and further modification of the reconstructed densities and pressures is unnecessary.

Similarly, the second-order source terms can be calculated as

$$\mathbf{S}^1_{i,j} = \mathbf{s}^{1,*}_{i-1/2,j} \mathbf{1}_{\{s_{M,i-1/2,j} \geqslant 0\}} + \mathbf{s}^{1,*}_{i+1/2,j} \mathbf{1}_{\{s_{M,i+1/2,j} < 0\}},$$

where $\mathbf{s}^{1,*}_{i+1/2,j}$ is defined as in (3.9), but with the values $\mathbf{W}_{i,j}$ and $\mathbf{W}_{i+1,j}$ replaced by $\mathbf{W}^E_{i,j}$ and $\mathbf{W}^W_{i+1,j}$ and a second-order equivalent value of parameter $\widetilde{\mathbf{B}}$. The source $\mathbf{S}^2_{i,j}$ in the y-direction is defined analogously. Observe that for smooth solutions, the discretized source $\mathbf{S}^1_{i,j}$ vanishes to truncation order with $(B^E_1)_{i,j} - (B^W_1)_{i+1,j}$. Hence, we need to add an extra term for second-order consistency. However, this term should vanish when $\mathbf{S}^1_{i,j}$ becomes significant at jumps (see e.g., [1] for an analogous situation). We suggest the following simple modification,

$$\widetilde{\mathbf{S}}^1_{i,j} = \mathbf{S}^1_{i,j} + \begin{pmatrix} 0 \\ \mathbf{B}_{i,j} + \widetilde{\mathbf{B}}_{i,j} \\ \mathbf{u}_{i,j} \cdot \mathbf{B}_{i,j} \\ \mathbf{u}_{i,j} \end{pmatrix} \frac{1}{\Delta x} D^x B^1_{i,j}.$$

The source term $\widetilde{\mathbf{S}}^2_{i,j}$ in the y-direction is defined analogously. Similar forms of the discrete source were found to be very stable in [53,19]. Note that $\widetilde{\mathbf{S}}^{1,2}_{i,j}$, are consistent second-order discretizations of the Godunov–Powell source terms $\mathbf{s}^{1,2}$.

The gravity source term $\mathbf{S}^g_{i,j}$ is defined by (3.23) and (3.25) (omitting the n-superscript in (3.25) for compatibility of notation). Note that (3.29) established that the source term (3.25) is second-order accurate.

3.2.4. Boundary conditions for the second-order scheme

The boundary is treated in the following way. We need to specify two layers of ghost cells in each direction for a second-order scheme. We have periodic boundary conditions in the x-direction, i.e., for $1 \leqslant j \leqslant N_y$ we have

$$\mathbf{W}_{0,j} = \mathbf{W}_{N_x,j}, \quad \mathbf{W}_{-1,j} = \mathbf{W}_{N_x-1,j}, \quad \mathbf{W}_{N_x+1,j} = \mathbf{W}_{1,j}, \quad \mathbf{W}_{N_x+2,j} = \mathbf{W}_{2,j}. \tag{3.38}$$

In the y-direction, we use extrapolated Neumann boundary conditions. In terms of the equilibrium variables, where $\mathbf{L}\rho_{i,j} = \log(\rho_{i,j})$ and $\mathbf{L}p_{i,j} = \log(p_{i,j})$, we take

$$\begin{aligned}
&\mathbf{L}\rho_{i,d} = \mathbf{L}\rho_{i,1} + \frac{(1+d)\Delta y}{H_{i,1}}, \quad \mathbf{L}\rho_{i,Ny+1+d} = \mathbf{L}\rho_{i,Ny} - \frac{(1+d)\Delta y}{H_{i,Ny}} \\
&\mathbf{u}_{i,d} = \mathbf{u}_{i,1+d}, \quad \mathbf{u}_{i,Ny+1+d} = \mathbf{u}_{i,Ny-d} \\
&\mathbf{L}p_{i,d} = \mathbf{L}_{i,1} + \frac{(1+d)\Delta y}{H_{i,1}}, \quad \mathbf{L}p_{i,N_y+1+d} = \mathbf{L}p_{i,N_y} - \frac{(1+d)\Delta y}{H_{i,N_y}} \\
&\mathbf{B}_{i,d} = \mathbf{B}_{i,1+d}, \quad \mathbf{B}_{i,N_y+1+d} = \mathbf{B}_{i,N_y-d},
\end{aligned} \tag{3.39}$$

for $1 \leqslant i \leqslant N_x$ and $d \in \{0,1\}$ in order to define all the values in the ghost cells. This amounts to using the extrapolated Neumann type boundary conditions of [18] for the primitive variables.

3.2.5. Time stepping

The standard scheme for a first-order approximation in time is the forward Euler time stepping, formally written

$$\mathbf{W}_{i,j}^{n+1} = \mathbf{W}_{i,j}^{n} + \Delta t^n \mathscr{F}_{i,j}^{n},$$

where $\mathscr{F}_i^n$ is defined in (3.32). For second-order schemes, we use the second-order strong stability preserving Runge-Kutta (SSP) time stepping (see [23])

$$\begin{aligned}
&\mathbf{W}_{i,j}^{*} = \mathbf{W}_{i,j}^{n} + \Delta t^n \mathscr{F}_{i,j}^{n}, \\
&\mathbf{W}_{i,j}^{**} = \mathbf{W}_{i,j}^{*} + \Delta t^n \mathscr{F}_{i,j}^{*}, \\
&\mathbf{W}_{i,j}^{n+1} = \frac{1}{2}(\mathbf{W}_{i,j}^{n} + \mathbf{W}_{i,j}^{**}).
\end{aligned}$$

The time step is determined by a standard CFL condition.

The properties of the second-order scheme are summarized in the theorem below,

Theorem 2. *Consider the scheme (3.32) approximating the system (2.5). This scheme has the following properties,*

(i) The scheme (3.32) is consistent with (2.5) and is second-order accurate.
(ii) The scheme (3.32) is well-balanced and preserves a discrete version of the steady state (2.11), i.e., given data satisfying

$$\mathbf{u}_{i,j} = 0, \quad \mathbf{B}_{i,j} = 0, \quad \rho_{i,j} = \rho_{i,j}^0 e^{\frac{-y_j}{H}}, \quad p_{i,j} = p_{i,j}^0 e^{\frac{-y_j}{H}}, \quad \text{for all } i \text{ and } j, \tag{3.40}$$

and any background field $\widetilde{\mathbf{B}}$, then the approximate solutions computed by (3.32) satisfy,

$$\frac{d}{dt}\mathbf{W}_{i,j} \equiv 0,$$

for all i and j.

Proof. The proof of consistency and second-order accuracy is a straightforward consequence of the design of the scheme (3.32) and can be easily checked. We prove the well-balancing property. Assume that the data satisfies (3.40), then observe that the data is constant along the x-direction. This implies that

$$\widetilde{\mathbf{F}}_{i+1/2,j} - \widetilde{\mathbf{F}}_{i-1/2,j} \equiv 0,$$

for all i and j. Furthermore $\mathbf{u}_{i,j}, \mathbf{B}_{i,j} \equiv 0$ implies that

$$D^x\mathbf{u}_{i,j}, D^y\mathbf{u}_{i,j}, \quad D^x\mathbf{B}_{i,j}, D^y\mathbf{B}_{i,j} \equiv 0,$$

for all i and j. This is true for the minmod, ENO and WENO reconstructions. Therefore all the reconstructed values of $\mathbf{u}$ and $\mathbf{B}$ are zero and the source terms $\widetilde{\mathbf{S}}^1$ and $\widetilde{\mathbf{S}}^2$ are zero for all i and j. A straightforward application of (3.40) leads to the following,

$$\begin{aligned}
&D^x\mathbf{L}\rho_{i,j} \equiv 0, \quad D^x\mathbf{L}p_{i,j} \equiv 0, \\
&D^y\mathbf{L}\rho_{i,j} \equiv \frac{-\Delta y}{H}, \quad D^y\mathbf{L}p_{i,j} \equiv \frac{-\Delta y}{H},
\end{aligned}$$

The above is true for all the three reconstructions, i.e. minmod (3.34), ENO (3.35) or WENO (3.36) reconstructions. Consequently, a simple calculation leads to the following reconstructed density and pressure,

$$\begin{aligned}
&\bar{\rho}_{i,j}(x,y) = \rho_0 e^{-y_j/H} e^{-(y-y_j)/H}, \\
&\bar{p}_{i,j}(x,y) = p_0 e^{-y_j/H} e^{-(y-y_j)/H}.
\end{aligned} \tag{3.41}$$

Hence, we can define $\rho_{i,j+1/2}$ and $p_{i,j+1/2}$ by

$$\begin{aligned}
&\rho_{i,j}^N = \rho_{i,j+1}^S = \rho_{i,j+1/2} = \rho_0 e^{-y_j/H} e^{\frac{-\Delta y}{2H}}, \\
&p_{i,j}^N = p_{i,j+1}^S = p_{i,j+1/2} = p_0 e^{-y_j/H} e^{\frac{-\Delta y}{2H}},
\end{aligned} \tag{3.42}$$

for all i and j. From consistency of the numerical flux, we obtain

$$\widetilde{\mathbf{G}}_{i,j+1/2} = \mathbf{G}\left(\rho^E_{i,j}, 0, 0, p^E_{i,j}, \rho^W_{i,j+1}, 0, 0, p^W_{i,j+1}, \widetilde{\mathbf{B}}_{i,j+1/2}\right) = \mathbf{g}\left(\rho^E_{i,j}, 0, 0, p^E_{i,j}\right)$$

and using (3.42), we obtain

$$\widetilde{\mathbf{G}}_{i,j+1/2} = (0, 0, p_{i,j+1/2}, 0, 0, 0, 0, 0). \tag{3.43}$$

Similarly an explicit evaluation of the gravitational source term in this case yields,

$$\mathbf{S}^g_{i,j} = \left\{0, 0, \frac{p_{i,j+1/2} - p_{i,j-1/2}}{\Delta y}, 0, 0, 0, 0, 0\right\}.$$

where using (3.23) leads to a value of $p_{i,j+1/2}$ defined in (3.42).

Therefore combining the above two expressions, we obtain

$$\frac{\widetilde{\mathbf{G}}_{i,j+1/2} - \widetilde{\mathbf{G}}_{i,j-1/2}}{\Delta y} = \mathbf{S}^g_{i,j}.$$

Inserting the above identity in (3.32) and using that both flux differences in the x-direction and the Godunov–Powell source terms vanish, leads to

$$\frac{d}{dt}\mathbf{W}_{i,j} \equiv 0,$$

for all i and j. Note that the reconstruction in equilibrium variables was absolutely essential in the above proof. □

4. Wave propagation: numerical experiments

We test the first-order (3.1) and second-order (3.32) schemes on a suite of numerical experiments. For the sake of comparison, we consider an *unbalanced* version of the first-order scheme similar to (3.1) based on the HLL three wave solver and upwind discretization of the Godunov–Powell source terms. This scheme does not use local hydrostatic reconstructions of density and pressure (3.23) and discretizes gravity by the simpler form

$$\widetilde{\mathbf{S}}^g_{i,j} = \{0, 0, 0, -\rho_{i,j}g, 0, 0, 0, -\rho_{i,j}u_{2,i,j}g\}. \tag{4.1}$$

Similarly, we consider a second-order version of the above *unbalanced* scheme based on a WENO reconstruction in the conservative variables, as opposed to the equilibrium variables of the scheme (3.32). Hence, we test the following five schemes:

H_3	First-order *unbalanced* HLL three wave solver,
H_{3WB}	well-balanced version of H_3 (3.1),
$H_{3WB}M$	Second-order well-balanced HLL three-wave solver (3.32) with Minmod reconstruction (3.34),
H_3W	Second-order *unbalanced* HLL three-wave solver with WENO reconstruction
$H_{3WB}W$	Second-order well-balanced HLL three wave solver (3.32) with WENO reconstruction (3.36).

The results with a well-balanced ENO scheme were very similar on most problems to either the $H_{3WB}M$ scheme or the $H_{3WB}W$ scheme and we omit them from the following presentation. The first order schemes are evolved with a CFL number of 0.45 and the second-order schemes use a CFL number of 0.9. In all our computations we set $\gamma = 5/3$.

Regarding the measurement of errors, if we have a reference solution available, then we define the relative error as

$$100 \times \frac{\|\alpha - \alpha_{\text{ref}}\|}{\|\alpha_{\text{ref}}\|},$$

where α is (a component of) the numerical approximation and α_{ref} is (the same component of) the reference solution, and $\|\cdot\|$ is some (usually L^1) norm.

4.1. Hydrodynamics: steady state

We begin with a numerical experiment with zero background magnetic field $\widetilde{\mathbf{B}}$. This idealized stellar atmosphere is modeled by a two dimensional spatial domain of $[0, 4] \times [0, 1]$. The initial conditions are given by the hydrodynamic steady state (2.11) and $\widetilde{\mathbf{B}} \equiv 0$ with a scale height of $H = 0.158$, initial pressure $p_0 = 1.13$ and gravitational constant $g = 2.74$. The parameters are chosen to approximate the dimensional parameters used in [6]. The simulation is carried out up to a time of $t = 1.8$. Here we will compare the performance of our schemes in preserving the steady state (2.11) to the *unbalanced* version of

these schemes. Our interest is measuring errors in preserving the steady state with respect to both the pressure (density) and the velocity. We compute relative percentage errors in pressure by

$$100 \times \frac{\|p - p_{\text{ref}}\|_{L^1}}{\|p_{\text{ref}}\|_{L^1}},$$

where p_{ref} is simply the steady state pressure (2.11). It is harder to compute relative errors in the velocity as the steady state velocity is $\mathbf{u} \equiv 0$. However, the velocity can be compared to the sound speed $a = \sqrt{\gamma p/\rho}$. Note that the steady state sound speed is a constant given by $a = \sqrt{\gamma g H}$ where g and H are the acceleration due to gravity and the scale height. A simple calculation with the constants considered here lead to $a = 0.85$. Therefore, we measure velocity errors by the following,

$$100 \times \frac{\|u_2\|_{L^1}}{a},$$

where we choose the velocity component u_2 for convenience. The numerical errors in L^1 for the pressure and the velocity (as calculated above) on a series of meshes are presented in Table 1. From this table, we see that using the *unbalanced* schemes H_3 and H_3W leads to errors in preserving the steady state pressure and velocity although they converge to zero when the mesh is refined. The first-order H_3 scheme has large errors and the rate of convergence is 1. The WENO based H_3W does a much better job with respect to steady state errors and the observed rate of convergence is close to 3. However, the errors (even with WENO scheme) are too large to allow for computations of very small perturbations of the steady state.

On the other hand, the well-balanced schemes perform much better. As proved in Theorems 1and 2, the well-balanced schemes preserve the steady state up to machine precision for both first and second-order schemes. This experiment serves to illustrate the contrast between *unbalanced* schemes are their well-balanced counterparts.

4.2. Hydrodynamics: wave propagation

The next step is to simulate hydrodynamic wave propagation. The computational domain is the same as in the previous experiment. The propagation of waves is initiated by sending in a sinusoidal (in time) sequence of waves from the bottom boundary, and letting them propagate across the domain and exiting at the top. The initial data is the hydrodynamic steady state (2.11) (with the background magnetic field $\tilde{\mathbf{B}} \equiv 0$). The waves are modeled by the following boundary conditions for the normal velocity at the bottom,

$$u^{2,n}_{i,\{0,-1\}} = \exp(-100(x_{i,\{0,-1\}} - 1.9)^2) c \sin(6\pi t^n). \tag{4.2}$$

Hence, we model the bottom boundary as a localized piston at $x = 1.9$. These waves move up through the domain and are modified by the pressure and gravity forces. We perform two different tests for this model. In the first one, we apply very small perturbations ($c = 3.0e^{-3}$). This test serves to illustrate the well-balancing properties of the schemes. Fig. 1 shows u_2 at time $t = 1.8$ for the small wave perturbations ($c = 3.0e^{-3}$) for an 800×200 mesh. The first-order H_{3WB} scheme is very dissipative. There is a tremendous difference between the first-order scheme and the second-order schemes. Additionally, we observe that the WENO scheme, (being formally third-order accurate) shows better accuracy than the Minmod reconstruction. Observe from Table 1 that the steady state velocity errors with the unbalanced H_3 and H_3W are either of the same order or orders of magnitude greater than the perturbations and it was not possible to resolve these very small waves for any of the *unbalanced* schemes. This illustrate the computational efficiency of well-balanced schemes in resolving small perturbations of the steady state.

Now, we increase the amplitude of the waves introduced at the bottom boundary (4.2) by two orders of magnitude with $c = 0.3$. In Fig. 2 we present the results for the first and second-order well-balanced schemes ($H_{3WB}, H_{3WB}M, H_{3WB}W$). We can see that the waves are resolved very well and there is a clear improvement in resolution from first to second-order schemes. Furthermore, the WENO scheme has better resolution than the minmod scheme.

Table 1
Percentage relative L^1 errors in p and u_2 for different schemes on different meshes. Left: unbalanced schemes, right: well-balanced schemes

H_3	H_3W	H_{3WB}	$H_{3WB}M$	$H_{3WB}W$	
% L^1-error in p					
100×25	4.9e+2	8.2e+0	7.0e − 13	1.1e − 12	1.6e − 13
200×50	1.6e+2	1.1e+0	3.7e − 14	7.2e − 14	5.7e − 14
400×100	6.7e+1	1.4e+1	4.8e − 13	4.3e − 13	2.7e − 13
800×200	3.0e+1	1.7e − 2	6.4e − 13	7.1e − 13	3.1e − 13
% L^1-error in p					
100×25	2.8e+1	9.7e − 1	7.0e − 13	1.1e − 12	1.6e − 13
200×50	1.5e+1	1.3e − 1	3.7e − 14	7.2e − 14	5.7e − 14
400×100	7.6e+0	1.7e − 2	4.8e − 13	4.3e − 13	2.7e − 13
800×200	2.4e+0	2.1e − 3	6.4e − 13	7.1e − 13	3.1e − 13

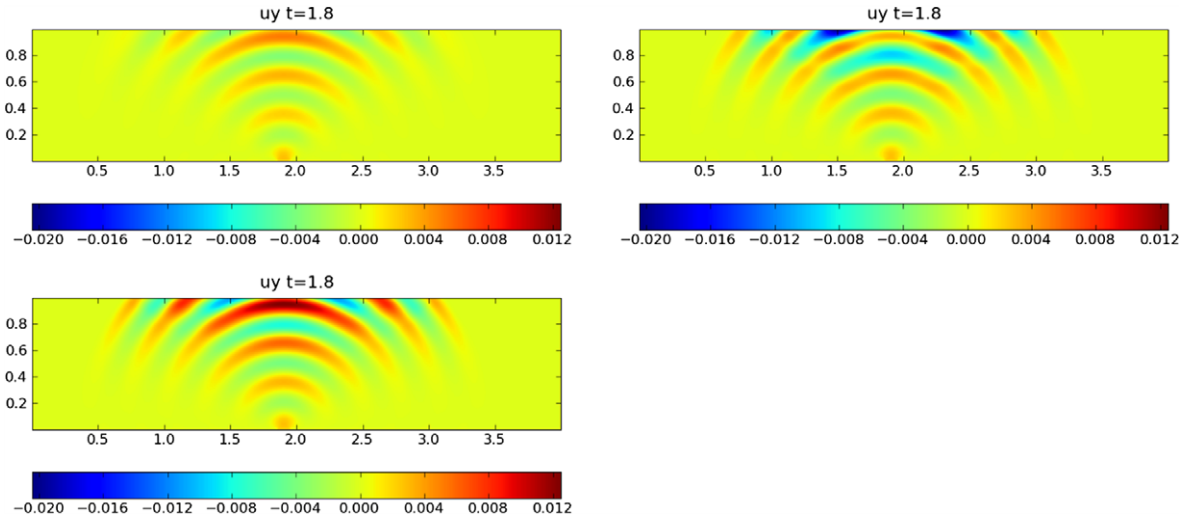

Fig. 1. The vertical velocity u^2 at $t = 1.8$ at a mesh resolution of 800×200 points for $c = 3.0e^{-3}$. Top left: H_{3WB}, top right: $H_{3WB}M$, left: $H_{3WB}W$.

The features are resolved quite well by the minmod and the WENO schemes. There was a small amount of reflections from the top boundary. However, the errors were quite small and did not affect the quality of the approximation in the interior.

A quantitative comparison of the three well-balanced schemes is provided in Table 2. The table shows relative percentage pressure errors in L^1 for the hydrodynamic wave propagation problem with strong waves (i.e. $c = 0.3$). In the absence of exact solution formulas, we use a reference solution computed on a very fine 3200×1600 mesh with the $H_{3WB}W$ scheme for calculating the errors. The table shows that the first-order H_{3WB} scheme is quite dissipative and the rate of convergence is clearly less than one. This is to be expected as the solution contains discontinuities in the form of sharp fronts and optimal convergence rates can only be computed for smooth solutions. The table also shows a large gain in accuracy with the $H_{3WB}M$ and $H_{3WB}W$ schemes. In particular, the WENO scheme is more accurate (at least on fine meshes) than the minmod scheme and leads to a convergence rate of close to 1.5 compared to the convergence rate of 1.2 with the minmod scheme. Although, using a reference solution does not provide rigorous evidence of convergence, it indicates that the well-balanced schemes resolve the solution quite well. Similar results were obtained for errors in the density and the velocity field.

4.3. Magnetohydrodynamics: steady state

A realistic model of the solar atmosphere must account for the magnetic field. We begin the magnetohydrodynamic tests by assessing the performance of different schemes in preserving a magnetic steady state of the form (2.4). As in the previous

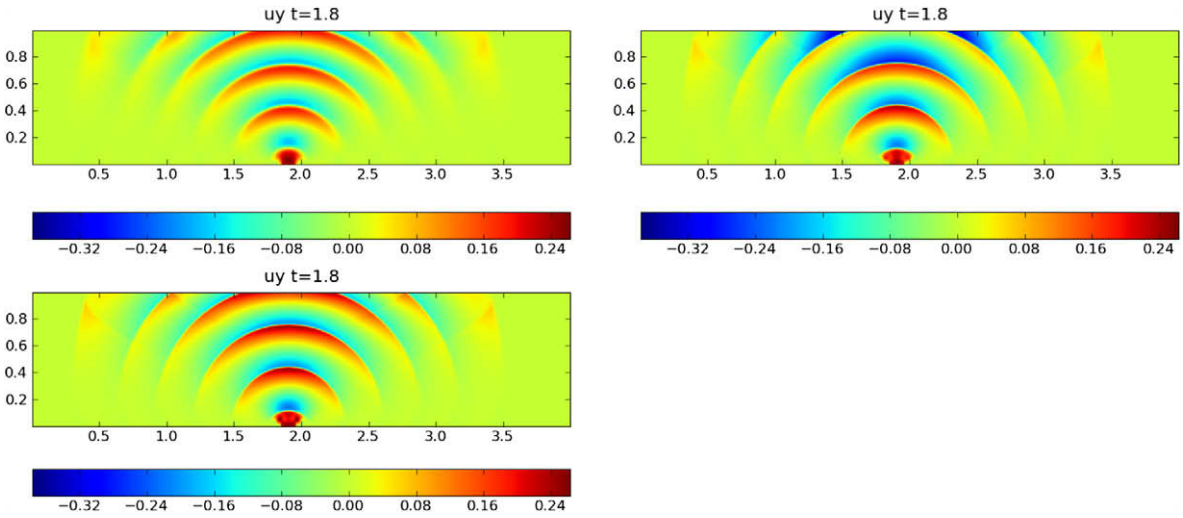

Fig. 2. The vertical velocity u^2 at $t = 1.8$ at a mesh resolution of 800×200 points for $c = 3.0e^{-1}$. Top left: H_{3WB}, top right: $H_{3WB}M$, left: $H_{3WB}W$.

Table 2
Relative percentage errors for the pressure in L^1 computed with respect to a fine mesh reference solution for the hydrodynamic wave propagation with strong waves at time $t = 0.8$ on a sequence of meshes.

M	H_{3WB}	rate	$H_{3WB}M$	rate	$H_{3WB}W$	rate
100×25	4.4e − 00		3.4e − 00		4.1e − 00	
200×50	3.5e − 00	0.33	2.1e − 00	0.69	2.3e − 00	0.83
400×100	2.5e − 00	0.48	1.1e − 00	0.93	1.0e − 00	1.20
800×200	1.6e − 00	0.64	5.1e − 01	1.11	3.5e − 01	1.52
1600×400	9.2e − 01	0.79	2.1e − 01	1.28	1.0e − 01	1.61

numerical experiment, the computational domain is $[0,4] \times [0,1]$. We consider the steady state (2.11) but with a non-trivial background magnetic field $\widetilde{\mathbf{B}}$. The background magnetic field is given by an expression of the form (2.13) in terms of a Fourier expansion. The Fourier coefficients are listed below. (The X in (2.13) is in this case equal to 4.)

$$\begin{aligned}\mathbf{FR} = \{f_0, f_1, \ldots, f_{14}\} = \{&0.552802906842, -0.696736253842, 0.908809914778, -0.813921192337, 0.360524088458,\\ &0.115217242296, -0.281974513346, 0.143723957761, 0.049431756210, -0.110095259045,\\ &0.053464228949, 0.011695376102, -0.028284735991, 0.013116555865, 0.001434008866\}.\end{aligned} \tag{4.3}$$

Note that the above magnetic field is quite complicated. It is designed to approximate a perturbed Gaussian profile magnetic field considered in [6]. This experiment was also considered in a recent paper [18]. The results of [18] indicated that it was much harder to compute steady states like (2.11) with magnetic field given by (2.13). In fact, all the finite volume schemes (with different combinations of boundary conditions) considered in [18] crashed on this problem. Hence, it is very interesting to see how the well-balanced schemes perform on this test case.

We compute with the three well-balanced schemes i.e. $H_{3WB}, H_{3WB}M$ and $H_{3WB}W$, and for the sake of comparison, we also compute with the two *unbalanced* schemes until $t = 1.8$ on a sequence of meshes. The relative percentage errors in L^1 (as calculated in Numerical experiment Section 4.1) for both the pressure and the velocity are given in Table 3. The table clearly shows that the well-balanced schemes preserve the steady state to machine precision whereas the *unbalanced schemes* lead to relatively large errors. The errors in both sets of schemes are comparable to the errors in preserving the hydrodynamic steady state (see Table 1). Hence, it is not possible to use *unbalanced schemes* for approximating very small perturbations of steady states.

4.4. Wave propagation: effect of the magnetic field

This test case is set up to illustrate the transition from hydrodynamics to MHD by observing the effect that magnetic fields have on wave propagation. The computational domain is $[0,2] \times [0,1]$ with the initial data corresponding to the steady state (2.11). The waves are modeled by the following boundary conditions for the normal velocity at the bottom,

$$\mathbf{u}^n_{i,\{0,-1\}} = c\frac{\mathbf{B}^n_{i,\{0,-1\}}}{|\mathbf{B}^n_{i,\{0,-1\}}|}\sin(6\pi t^n)\mathbf{1}_{\{[1.85,1.95]\}} \tag{4.4}$$

with $c = 3e^{-1}$. Hence, we model the bottom boundary as a localized piston in the interval $[1.85, 1.95]$. We consider the simple homogeneous background field $\widetilde{\mathbf{B}}$ given by

$$\widetilde{B}_2 = \mu, \quad \widetilde{B}_1 = \widetilde{B}_3 = 0, \tag{4.5}$$

with a constant μ that we vary between each experiment. A crucial parameter is the plasma β given by

Table 3
Percentage relative L^1 errors in p and u_2 for different schemes on different meshes. Left unbalanced schemes. Right well-balanced schemes.

H_3	H_3W	H_{3WB}	$H_{3WB}M$	$H_{3WB}W$	
% L^1-*error in p*					
100×25	3.5e+2	6.3e+0	9.8e − 20	2.5e − 18	7.9e − 17
200×50	1.2e+2	8.2e − 1	1.6e − 18	3.6e − 18	4.1e − 16
400×100	4.9e+1	1.0e − 1	2.8e − 18	3.5e − 18	2.6e − 15
800×200	2.2e+1	1.3e − 2	4.6e − 18	1.4e − 17	2.0e − 14
% L^1-*error in p*					
100×25	2.0e+1	6.9e − 1	7.0e − 13	1.1e − 12	1.6e − 13
200×50	9.8e+0	8.6e − 2	3.7e − 14	7.2e − 14	5.7e − 14
400×100	4.8e+0	1.0e − 2	4.8e − 13	4.3e − 13	2.7e − 13
800×200	2.4e+0	1.3e − 3	6.4e − 13	7.1e − 13	3.1e − 13

$$\beta = \frac{2p}{\mathbf{B}^2}. \tag{4.6}$$

The parameter β measures the relative strength of the thermal pressure to the magnetic field and is crucial in determining the dynamics of the plasma. We show results on a 400×200 mesh at time $t = 0.54$, computed with the $H_{3WB}W$ scheme in Fig. 3. Three different values of μ: 0, 1 and 5 are chosen to illustrate of the effect of increasing the magnetic field strength. The magnetic field lines are shown in white and the β isolines are shown in black. The figure illustrates the role of the magnetic field. For $\mu = 0$ (hydrodynamics), the waves simply radiate outward at the constant speed of sound. Before discussing the numerical results for the configurations with magnetic fields, we describe some terminology: the waves corresponding to the eigenvalues $\lambda_{1,8}$ in (2.10) are called *fast waves*. Similarly, waves corresponding to the eigenvalues $\lambda_{3,6}$ are called *slow waves*. Clearly, the fast waves have much higher speed than the slow waves. Furthermore, the plasma velocity in the direction of the magnetic field only shows the presence of slow waves ([6]) whereas the velocity in the direction perpendicular to the magnetic field shows both fast as well as slow waves. In a stratified magneto-atmosphere (see the structure of (2.11), (2.13) and (4.3)), the pressure and the density decay exponentially with height whereas the magnetic field (at least its constant mode) remains approximately constant. Hence, a pressure dominated flow (with $\beta \gg 1$) at the bottom of the domain can change into a magnetically dominated flow (with $\beta \ll 1$) near the top of the domain. This implies that gas pressure and magnetic fields play different roles in different parts of the domain. Furthermore, the region $\beta \approx 1$ is very interesting in nature, since $\beta = 1$ corresponds to the well known *triple point* of MHD ([5]). This region is characterized by the fact that the fast and slow (also the Alfvén) eigenvalues almost coincide. The brief description above (a more detailed one can be found in [6]) serves to illustrate the complexity of the physics underlying wave propagation in stellar atmospheres, and the considerable numerical challenges that must be overcome to model this.

In Fig. 3 we present the velocity in the direction of the magnetic field. Given the planar magnetic field (4.5), this reduces to the velocity in y-direction. For $\mu = 1$, the magnetic field compresses the wave and its outward radial spread is reduced considerably. This should be contrasted with the hydrodynamic case. The compression increases considerably by increasing the magnetic field strength to $\mu = 5$. In this case, the velocity is completely focused by the magnetic field.

Another significant feature is the role of the plasma β. The triple line $\beta = 1$ serves to convert fast waves into a combination of fast and slow waves [6]. This phenomenon is illustrated in Fig. 4 where the velocity in the direction perpendicular to the magnetic field (the velocity in x-direction for this planar magnetic field) is shown. We show the results with the WENO scheme on a 400×200 mesh and with $\mu = 1$ at three different times. This particular magnetic field is chosen because it has a $\beta = 1$ isoline lying within the computational domain. Thus, this example shows the effect of both the gas pressure as well as the magnetic field. As soon as a fast wave hits the $\beta = 1$ isoline, mode conversion takes place and it is converted into a combination of fast and slow waves. Furthermore, the decreasing values of β imply that velocity of the fast waves increases quite rapidly after crossing the $\beta = 1$ isoline. This vertical increase of the fast wave speed in the low β region forces the fast waves to turn towards the high β region near the top boundary. This *turning* behavior is demonstrated quite well in right most panel of Fig. 4 and is physical [6]. The above results show that there are many interesting physical effects accompanying wave propagation in the presence of magnetic fields.

4.5. Wave propagation: weak magnetic fields

The above numerical experiment sets the stage for introducing more complicated background magnetic fields. We consider (2.4) with the steady state (2.11) as the initial data. The background magnetic field $\tilde{\mathbf{B}}$ is given in terms of the expansion (2.13) with Fourier coefficients given by the vector **FR**/3 where **FR** is defined in (4.3). This magnetic field is called *weak* in analogy with the terminology in [6]. The computational domain is $[0, 4] \times [0, 1]$.

We use the well-balanced schemes to compute to above configuration with two different perturbations. First, we consider a very weak perturbation of type (4.4) with magnitude $c = 3e^{-3}$. This test illustrates the well-balancing of the schemes. The results with all the three schemes $H_{3WB}, H_{3WB}M$ and $H_{3WB}W$ on a 800×200 mesh at time $t = 0.9$ are presented in Fig. 5. We

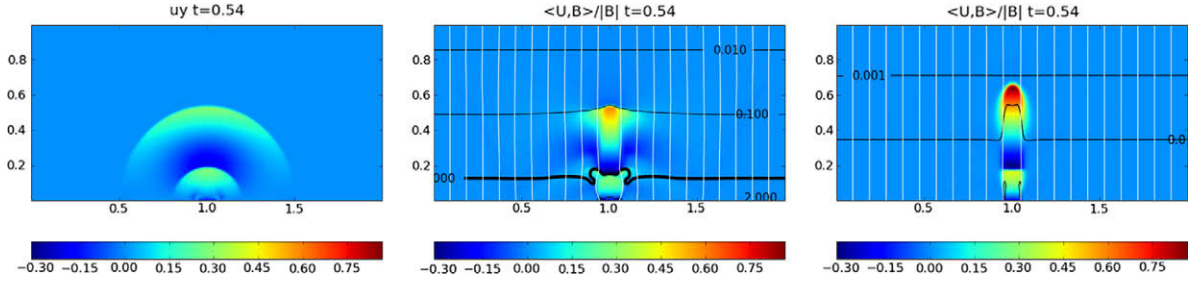

Fig. 3. Results for the simple magnetic field (4.5) with the WENO reconstruction at $t = 0.54$ on a 400×200 mesh. The magnetic field lines are in white and the β-isolines are in black, with thicker lines at $\beta = 1$. The figures show the velocity in the direction of the magnetic field. The magnetic field strength increases from left to right: left: $\mu = 0$, center: $\mu = 1$, right: $\mu = 5$.

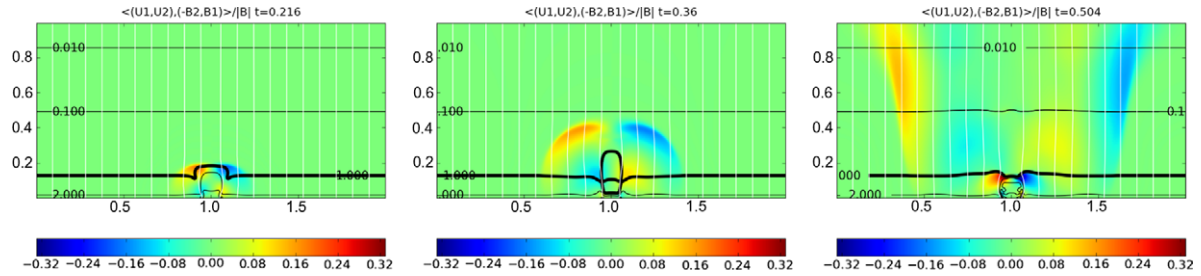

Fig. 4. Velocity perpendicular to the magnetic field for the simple magnetic field (4.5) with $\mu = 1$ and with the WENO reconstruction at different times on a 400×200 mesh. The magnetic field lines are white and the isolines of β black. Left:$t = 0.216$, center: $t = 0.36$, right: $t = 0.50$.

show both the component of the velocity field parallel to the magnetic field and the component perpendicular to it. Observe that all the three schemes are able to capture the small perturbations. This is quite challenging as the schemes need to preserve the steady state (2.11) with this complex magnetic field to machine precision in order to capture these small waves. The figure shows that the WENO scheme is most accurate and the first-order scheme is most dissipative. Furthermore, the complex physics is nicely resolved by all the three schemes. The velocity in the direction of the magnetic field shows the presence of the slow waves whereas the perpendicular component shows both fast and slow waves (observe that the leading fast wave has already reached the boundary at this time instant whereas the leading slow wave is still quite far from the top boundary). Note that the $\beta = 1$ isoline is at the center of the domain. The mode conversion described in the previous experiment is quite clearly seen.

A second set of computations with the above configuration involves a much stronger perturbation of the type (4.4) with magnitude $c = 3e^{-1}$. Thus the perturbation is two orders of magnitude greater than the one considered before. The results with all the three schemes at time $t = 0.9$ are shown in Fig. 6. The results are obtained on a 800×200 mesh. The qualitative

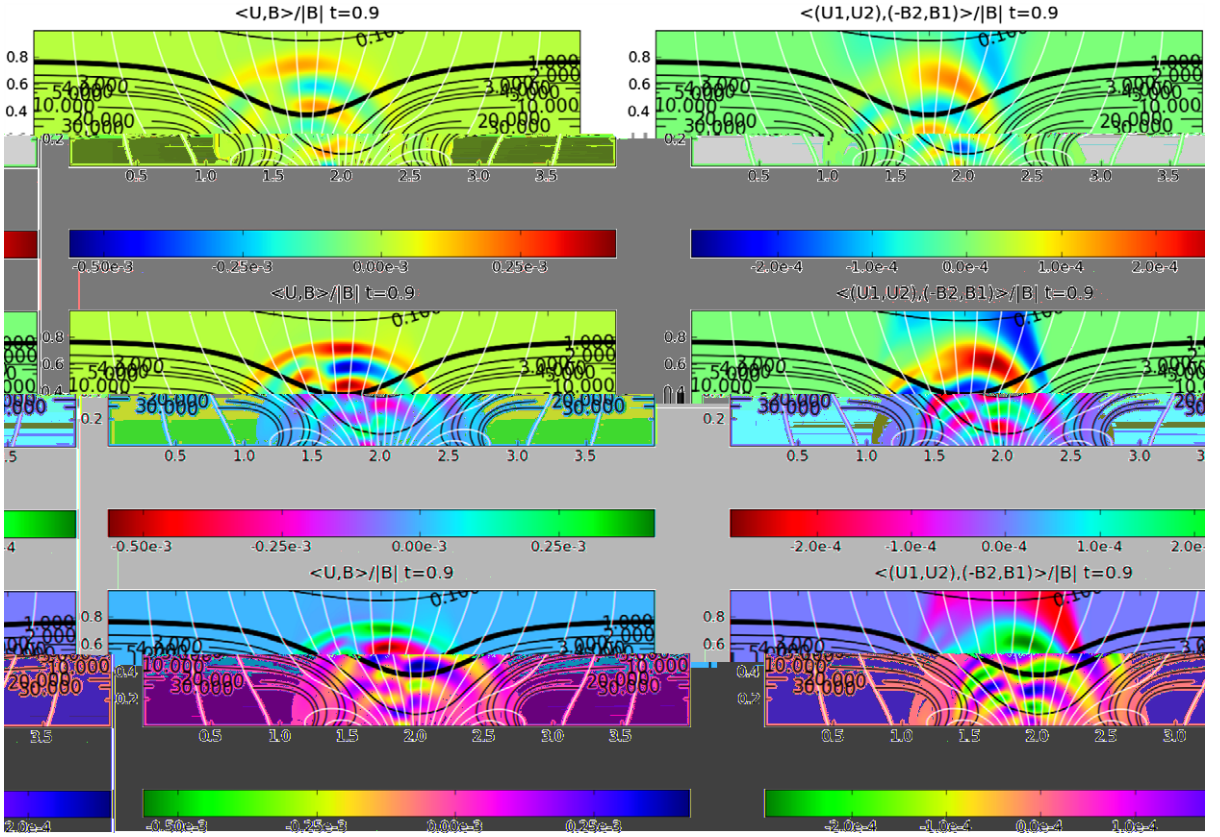

Fig. 5. Results for the weak magnetic background with small wave perturbations ($c = 3e^{-3}$) at $t = 0.9$ on a 800×200 mesh. The magnetic field lines are shown in white and the isolines of β in black. The left column shows the speed in the direction of the magnetic field lines and the right column shows the speed perpendicular to the magnetic field lines. Top row: H_{3WB}, middle row: $H_{3WB}M$, bottom row: $H_{3WB}W$.

features shown in Fig. 6 are similar to those presented in Fig. 5. The main differences are: the fast waves are much faster now and are exiting the top boundary at this instant of time. The turning behavior of the fast waves is quite pronounced. Another difference in this case is the observation that the magnetic field is being distorted quite strongly by the wave. This is to be expected as the magnetic field is not very strong and the waves have reasonably large magnitude. Note that the slow waves continue to spread radially outward as the magnetic field is not strong enough to focus them. At the level of schemes, all the three schemes resolve the complex physics quite well and allow us to deduce quantitative as well as qualitative conclusions on the nature of the wave propagation.

A quantitative comparison of the three well-balanced schemes is provided in Table 4 where we display relative percentage errors of the pressure in the L^1 norm. The errors are computed using a fine 3200×1600 mesh reference solution. Table 4 justifies some of the qualitative comparisons between the schemes. The first-order scheme is very dissipative and the rate of convergence approaches 0.8 whereas the $H_{3WB}M$ and $H_{3WB}W$ schemes are much more accurate. The WENO scheme has a rate of convergence close to 1.7 compared to the rate of 1.3 for the minmod scheme showing that the WENO scheme is more accurate.

4.6. Wave propagation: strong magnetic fields

We consider the same configuration as in the previous experiment. However, we increase the strength of the background magnetic field (2.13) by considering Fourier coefficients given by (4.3). Thus, the strength of the magnetic field is increased three times compared with the previous numerical experiment. This field is called the *strong* magnetic field. We begin with a very small perturbation of the type (4.4) with $c = 3e^{-3}$ to test the well-balancing properties of the schemes. The parallel and perpendicular components (to the direction of the magnetic field) of the velocity field at a resolution of 800×200 points are shown in Fig. 7. All the three schemes are able to capture the small perturbations quite accurately. The first-order scheme is dissipative, but the minmod and WENO schemes compute much sharper wave fronts. Furthermore, there are considerable differences in the behavior of the waves compared with the numerical experiment with a weaker magnetic field. The waves in direction of the magnetic field are much more focused by the magnetic field. This is to be expected as the magnetic field is stronger (see Fig. 3 for the planar magnetic field case). Also the fast waves are considerably faster in this case, given the

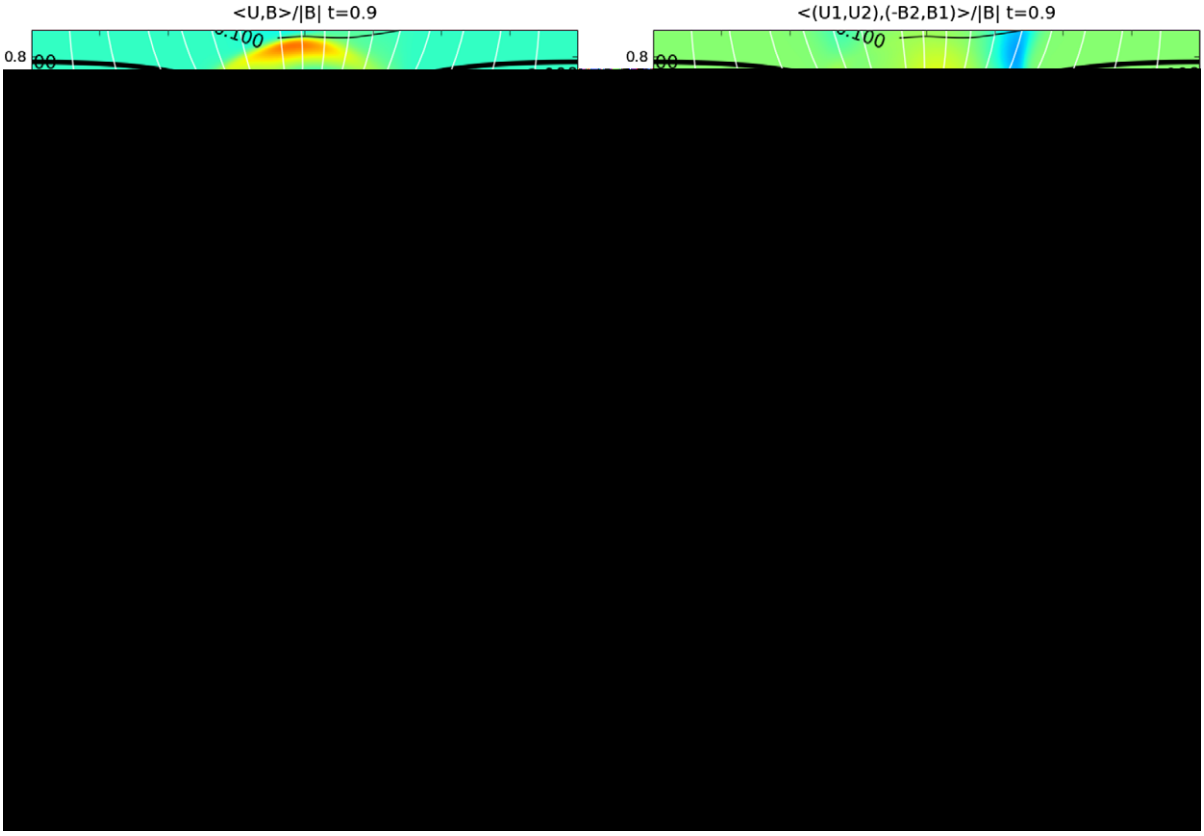

Fig. 6. Results for the weak magnetic background at $t = 0.9$ on a 800×200 mesh for $c = 3e^{-1}$. The magnetic field lines are shown in white and the isolines for β in black. The left column shows the speed in the direction of the magnetic field lines and the right column shows the speed perpendicular to the magnetic field lines. Top row: H_{3WB}, middle row: $H_{3WB}M$, bottom row: $H_{3WB}W$.

Table 4
Relative percentage errors for the pressure in L^1 computed with respect to a fine mesh reference solution for the magnetohydrodynamic wave propagation with the weak magnetic field and strong waves at time $t = 0.8$ on a sequence of meshes.

M	H_{3WB}	rate	$H_{3WB}M$	rate	$H_{3WB}W$	rate
100×25	3.0e − 00		2.1e − 00		3.2e − 00	
200×50	2.6e − 00	0.23	1.2e − 00	0.80	1.5e − 00	1.09
400×100	1.8e − 00	0.53	5.5e − 01	1.13	5.5e − 01	1.49
800×200	1.1e − 00	0.71	2.2e − 01	1.32	1.7e − 01	1.70
1600×400	6.2e − 01	0.82	9.7e − 02	1.27	6.8e − 02	1.69

stronger magnetic field. Hence, the maximum eigenvalues in (2.10) corresponding to the fast waves are larger. Consequently, the turning of the fast waves at the top boundary is more pronounced. The accurate numerical resolution of the complex phenomena with very small amplitudes illustrates the robustness of the well-balanced schemes. We consider the same configuration as above but increase the perturbation (4.4) by two orders of magnitude with $c = 3e^{-1}$. The results are shown in Fig. 8. The results are qualitatively similar to those observed in Fig. 7. The fast waves travel even faster now and the turning at the top boundary is more pronounced. Furthermore, the turned fast waves hit the $\beta = 1$ isoline and some of their energy is converted into slow waves. These slow waves are visible in the right hand side of the domain as very small waves in the direction parallel to the magnetic field.

A quantitative comparison of the three well-balanced schemes in this case is provided in Table 5 where we display relative percentage errors of the pressure in the L^1 norm. The errors are computed using a fine 3200×1600 mesh reference solution. Table 5 is very similar to Table 4 for the weak magnetic fields. The first-order scheme is very dissipative and the rate of convergence approaches 0.7 whereas the $H_{3WB}M$ and $H_{3WB}W$ schemes are much more accurate. The WENO scheme has a rate of convergence close to 1.45 compared to the rate of 1.15 for the minmod scheme showing that the WENO scheme is more accurate. Furthermore, the errors are larger in this case than when the magnetic field is weak. The rates of convergence with all the schemes are not optimal as the solution contains discontinuities, propagating as sharp fronts.

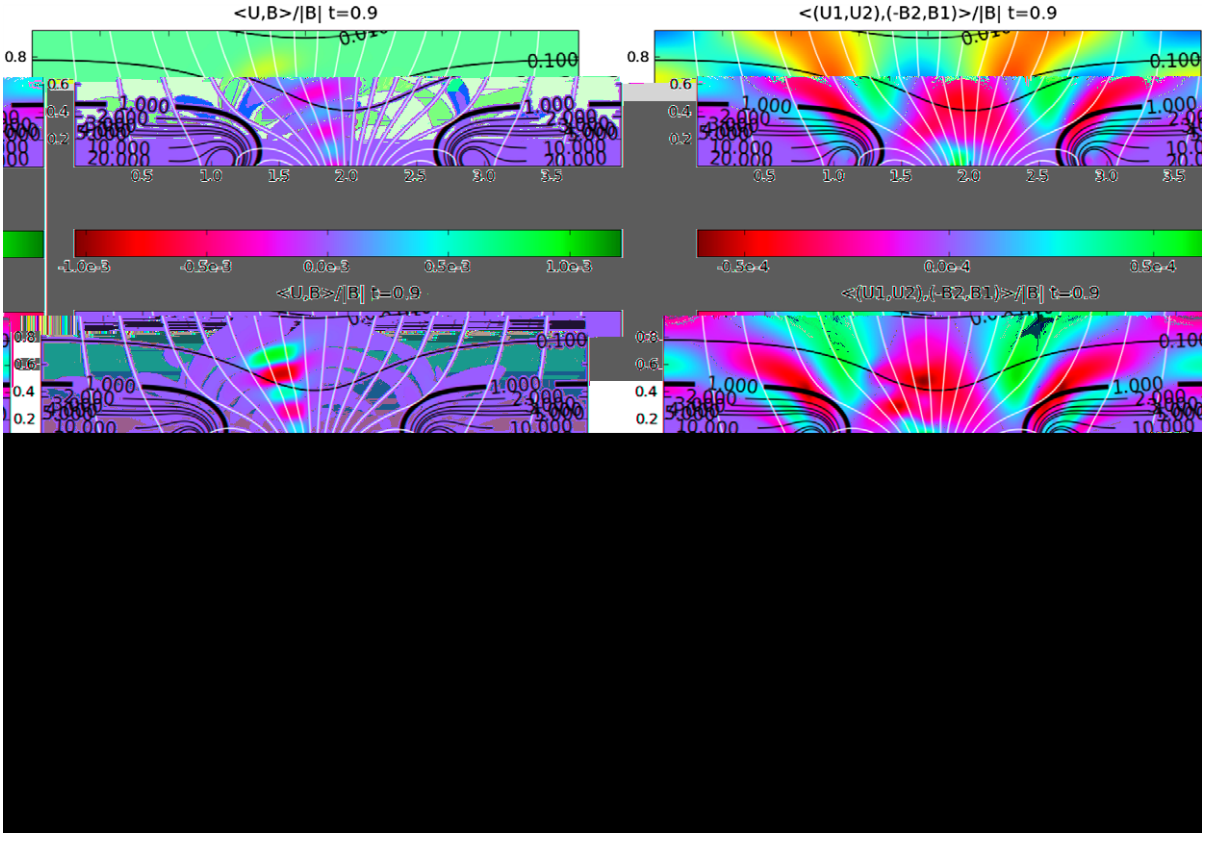

Fig. 7. Results for the strong magnetic background with small wave perturbations ($c = 3e^{-3}$) at $t = 0.9$ on a 800×200 mesh. The magnetic field lines are shown in white and the β-lines in black. The left column shows the speed in the direction of the magnetic field lines and the right column shows the speed perpendicular to the magnetic field lines. Top row: H_{3WB}, middle row: $H_{3WB}M$, bottom row: $H_{3WB}W$.

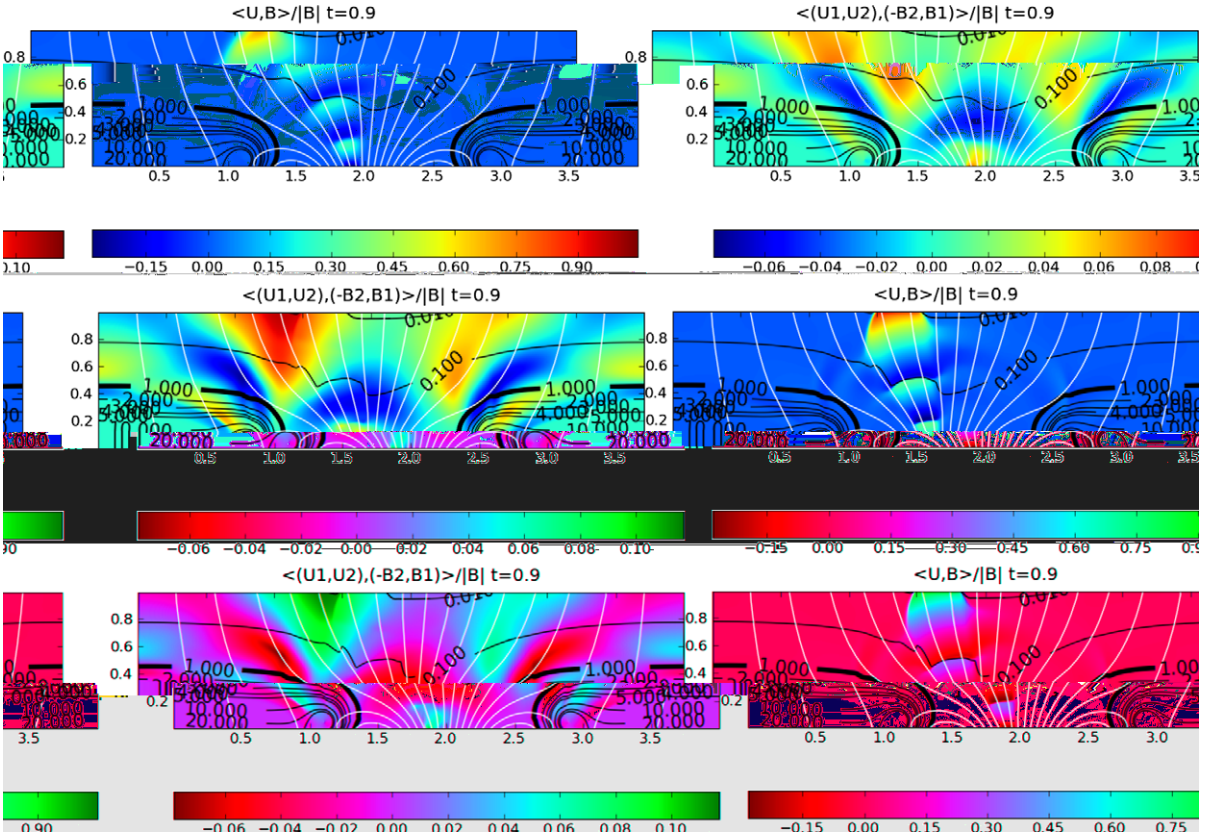

Fig. 8. Results for the strong magnetic background at $t = 0.9$ on a 800×200 mesh for $c = 3e^{-1}$. The magnetic field lines are shown in white and the isolines of β in black. The left column shows the speed in the direction of the magnetic field lines and the right column shows the speed perpendicular to the magnetic field lines. Top row: H_{3WB}, middle row: $H_{3WB}M$, bottom row: $H_{3WB}W$.

Table 5
Relative percentage errors for the pressure in L^1 computed with respect to a fine mesh reference solution for the magnetohydrodynamic wave propagation with the strong magnetic field and strong waves at time $t = 0.8$ on a sequence of meshes.

M	H_{3WB}	rate	$H_{3WB}M$	rate	$H_{3WB}W$	rate
100×25	3.6e − 00		2.7e − 00		3.3e − 00	
200×50	2.9e − 00	0.31	1.5e − 00	0.84	1.8e − 00	0.87
400×100	2.1e − 00	0.47	7.4e − 01	0.96	8.0e − 01	1.17
800×200	1.4e − 00	0.58	3.4e − 01	1.19	2.8e − 01	1.51
1600×400	8.4e − 01	0.73	1.5e − 01	1.12	9.8e − 02	1.45

5. Conclusion

We consider numerical simulations of wave propagation in an idealized stellar atmosphere. The model consists a reformulated ideal MHD system based on the Godunov–Powell form, together with an embedded steady magnetic field. The resulting equations are balance laws with gravity source terms and background magnetic fields playing the role of a parameter function. The system possesses interesting isothermal steady states. Waves are modeled as small perturbations of these steady states.

The system is simulated by finite volume schemes based on HLL three wave approximate Riemann solvers and upwind discretizations of the Godunov–Powell source term. The scheme is well-balanced by using local hydrostatic reconstructions of the density and pressure and a suitable discretization of the gravity source term. Second-order accurate schemes are designed by considered suitable minmod and WENO reconstructions. The reconstructions are performed in terms of *equilibrium* variables to ensure well-balancing.

The resulting schemes are high-order accurate, stable and well-balanced. They are validated on a large suite of numerical experiments. The underlying physical phenomena are quite complex and involve multiple scales and parameters. The

schemes perform very well and are able to resolve very small perturbations as well as the complex phenomena to a high degree of accuracy.

Future projects include employing the schemes of this paper on more realistic three-dimensional configurations with background magnetic fields and perturbations derived from observed data. Additional physical effects need to be included in order to increase the range of application of the models considered here. We plan to consider non-isothermal steady states, and to add effects of radiation in order to model stellar atmospheres in a more realistic manner. The extension to non-isothermal steady states requires non-trivial modifications of the ideas presented here and is considered in a forthcoming paper [20].

References

[1] E. Audusse, F. Bouchut, M.O. Bristeau, R. Klien, B. Perthame, A fast and stable well-balanced scheme with hydrostatic reconstruction for shallow water flows, SIAM J. Sci. Comput. 25 (6) (2004) 2050–2065.
[2] D.S. Balsara, D. Spicer, A staggered mesh algorithm using high order Godunov fluxes to ensure solenoidal magnetic fields in magnetohydrodynamic simulations, J. Comp. Phys. 149 (2) (1999) 270–292.
[3] T.J. Barth, Numerical methods for gas dynamics systems, in: D. Kröner, M. Ohlberger, C. Rohde (Eds.), An Introduction to Recent Developments in Theory and Numerics for Conservation Laws, Springer, 1999.
[4] Christophe Berthon, Stability of the MUSCL Schemes for the Euler Equations, Commun. Math. Sci. 3 (2) (2005) 133–157.
[5] D. Biskamp, Nonlinear magnetohydrodynamics, Cambridge Monographs on Plasma Physics, Cambridge University Press, 1993.
[6] T.J. Bogdan et al, Waves in the magnetized solar atmosphere II: waves from localized sources in magnetic flux concentrations, Astrophys. J. 599 (2003) 626–660.
[7] F. Bouchut, C. Klingenberg, K. Waagan, A multi-wave HLL approximate Riemann solver for ideal MHD based on relaxation I – theoretical framework, Numer. Math. 108 (1) (2007) 7–42.
[8] F. Bouchut, C. Klingenberg, K. Waagan, A multi-wave HLL approximate Riemann solver for ideal MHD based on relaxation II – Numerical experiments, Numerische Mathemat (2010), in press.
[9] J.U. Brackbill, D.C. Barnes, The effect of nonzero div$B$ on the numerical solution of the magnetohydrodynamic equations, J. Comp. Phys. 35 (1980) 426–430.
[10] P. Cargo, G. Gallice, Roe matrices for ideal MHD and systematic construction of Roe matrices for systems of conservation laws, J. Comp. Phys 136 (2) (1997) 446–466.
[11] M. Castro, J.M. Gallardo, C. Parés, High order finite volume schemes based on reconstruction of states for solving hyperbolic systems with non-conservative products, Math. Comp. 75 (2006) 1103–1134.
[12] W. Dai, P.R. Woodward, A simple finite difference scheme for multi-dimensional magnetohydrodynamic equations, J. Comp. Phys. 142 (2) (1998) 331–369.
[13] A. Dedner, F. Kemm, D. Kröner, C.D. Munz, T. Schnitzer, M. Wesenberg, Hyperbolic divergence cleaning for the MHD equations, J. Comp. Phys. 175 (2002) 645–673.
[14] B. Einfeldt, On the Godunov type methods for gas dynamics, SIAM. J. Num. Anal. 25 (2) (1988) 294–318.
[15] C. Evans, J.F. Hawley, Simulation of magnetohydrodynamic flow: A constrained transport method, Astrophys. J. 332 (1998) 659.
[16] F. Fuchs, K.H. Karlsen, S. Mishra, N.H. Risebro, Stable Upwind Schemes for the Magnetic Induction Equation, Math. Model. Num. Anal. 43 (2009) 825–852.
[17] F. Fuchs, S. Mishra, N.H. Risebro, Splitting based finite volume schemes for the ideal MHD equations, J. Comp. Phys. 228 (3) (2009) 641–660.
[18] F. Fuchs, A.D. McMurry, S. Mishra, N.H. Risebro, K. Waagan, Finite volume schemes for wave propagation in stratified magneto-atmospheres, Commun. Comput. Phys. 7 (2010) 473–509.
[19] F. Fuchs, A.D. McMurry, S. Mishra, N.H. Risebro, K. Waagan, Approximate Riemann solver based high-order finite volume schemes for the Godunov–Powell form of ideal MHD equations in multi-dimensions, Preprint, Submitted, available from folk.uio.no/siddharm/art32.pdf.
[20] F. Fuchs, A.D. McMurry, S. Mishra, N.H. Risebro, K. Waagan, Well-balanced high-order accurate finite volume schemes for simulating waves in three-dimensional non-isothermal magneto-atmospheres, (2010), submitted for publication.
[21] S.K. Godunov, The symmetric form of magnetohydrodynamics equation, Num. Meth. Mech. Cont. Media 1 (1972) 26–34.
[22] K.F. Gurski, An HLLC-type approximate Riemann solver for ideal Magnetohydrodynamics, SIAM. J. Sci. Comput. 25 (6) (2004) 2165–2187.
[23] S. Gottlieb, C.W. Shu, E. Tadmor, High order time discretizations with strong stability property, SIAM. Review 43 (2001) 89–112.
[24] A. Harten, B. Engquist, S. Osher, S.R. Chakravarty, Uniformly high order accurate essentially non-oscillatory schemes, J. Comput. Phys. (1987) 231–303.
[25] K.H. Karlsen, S. Mishra, N.H. Risebro, A new class of well-balanced schemes for conservation laws with source terms, Math. Comput. 78 (265) (2009) 55–78.
[26] K.H. Karlsen, S. Mishra, N.H. Risebro, Semi-Goudunov schemes for multiphase flows in porous media, Appl. Num. Math. 59 (9) (2009) 2322–2336.
[27] D. KRöner, M.D. Thanh, Numerical solutions to compressible flows in a nozzle with variable cross-section, SIAM J. Numer. Anal. 43 (2) (2005) 796–824.
[28] P.G. LeFloch, M.D. Thanh, The Riemann problem for fluid flows in a nozzle with discontinuous cross-section, Commun. Math. Sci. 1 (4) (2003) 763–797.
[29] R.J. LeVeque, Finite Volume Methods for Hyperbolic Problems, Cambridge university press, Cambridge, 2002.
[30] R.J. LeVeque, Balancing source terms and flux gradients in high-resolution Godunov methods: The Quasi-steady wave propagation algorithm, J. Comput. Phys. 146 (1998) 346–365.
[31] T.J. Linde, A practical, general-purpose two-state HLL Riemann solver for hyperbolic conservation laws, Int. J. Num. Methods Fluids 40 (3–4) (2002) 391–402.
[32] P. Londrillo, L. del Zanna, On the divergence free condition in Godunov-type schemes for ideal magnetohydrodynamics: The upwind constrained transport method, J. Comput. Phys. 195 (2004) 17–48.
[33] B. Marder, A method for incorporating Gauss' law into electromagnetic pic codes, J. Comput. Phys. 68 (1) (1987) 48–55.
[34] A. Mignone et al, Pluto: A numerical code for computational astrophysics, Astrophys. J. Suppl. 170 (2007) 228–242.
[35] S. Mishra, Analysis and numerical approximation of conservation laws with discontinuous coefficients, Ph.D Thesis, IISc, Bangalore, India, 2005, p. 260.
[36] T. Miyoshi, K. Kusano, A multi-state HLL approximate Riemann solver for ideal magnetohydrodynamics, J. Comp. Phys. 208 (1) (2005) 315–344.
[37] S. Noelle, N. Pankratz, G. Puppo, J. Natvig, Well-balanced finite volume schemes of arbitrary order of accuracy for shallow water flows, J. Comput. Phys. 213 (2006) 474–499.
[38] T.J. Poinsot, S.K. Lele, Boundary conditions for direct simulations of compressible viscous flows, J. Comp. Phys. 101 (1992) 104–129.
[39] K.G. Powell, An approximate Riemann solver for magnetohydrodynamics (that works in more than one space dimension), Technical report, 94-24, ICASE, Langley, VA, 1994.
[40] K.G. Powell, P.L. Roe, T.J. Linde, T.I. Gombosi, D.L. De zeeuw, A solution adaptive upwind scheme for ideal MHD, J. Comput. Phys 154 (2) (1999) 284–309.
[41] P.L. Roe, D.S. Balsara, Notes on the eigensystem of magnetohydrodynamics, SIAM J. Appl. Math. 56 (1) (1996) 57–67.
[42] C.S. Rosenthal et al, Waves in the magnetized solar atmosphere I: Basic processes and internetwork oscillations, Astrophys. J. 564 (2002) 508–524.

[43] J. Rossmanith, A wave propagation method with constrained transport for shallow water and ideal magnetohydrodynamics, Ph.D Thesis, University of Washington, Seattle, 2002.
[44] D.S. Ryu, F. Miniati, T.W. Jones, A. Frank, A divergence free upwind code for multidimensional magnetohydrodynamic flows, Astrophys. J. 509 (1) (1998) 244–255.
[45] C.W. Shu, S. Osher, Efficient implementation of essentially non-oscillatory schemes-II, J. Comput. Phys. 83 (1989) 32–78.
[46] J.M. Stone et al, Athena: A new code for astrophysical MHD, Astrophys. J. Suppl. 178 (2008) 137–177.
[47] T. Tanaka, Finite volume TDV scheme on an unstructured grid system for three-dimensional simulations of inhomogenous system including strong background potential field, J. Comput. Phys. 111 (1994) 381.
[48] K.W. Thompson, Time dependent boundary conditions for hyperbolic systems, J. Comput. Phys. 68 (1987) 1–24.
[49] M. Torrilhon, Locally divergence preserving upwind finite volume schemes for magnetohydrodynamic equations, SIAM J. Sci. Comput. 26 (4) (2005) 1166–1191.
[50] M. Torrilhon, Uniqueness conditions for Riemann problems of ideal magnetohydrodynamics, J. Plasma. Phys. 69 (3) (2003) 253–276.
[51] G. Toth, The div$B = 0$ constraint in shock capturing magnetohydrodynamics codes, J. Comput. Phys. 161 (2000) 605–652.
[52] B. Van Leer, Towards the ultimate conservative difference scheme, V. J. Comput. Phys. 32 (1979) 101–136.
[53] K. Waagan, A positive MUSCL-Hancock scheme for ideal MHD, Comp. Phys. 228 (23) (2009) 8609–8626.